FACULDADE DE ENGENHARIA DA UNIVERSIDADE DO PORTO

Thermal Management of the Battery Pack in Electric Vehicles

Pedro Miguel Santos Ramos

Mestrado em Engenharia Mecânica

UNIPR Supervisor: Fabio Bozzoli

FEUP Supervisor: Eliseu Monteiro

July 28, 2024

Abstract

The big investment in electric vehicle (EV) industry has been promoted by the objective of reducing the greenhouse gases emissions, and the goals established in COP28 to reduce the mobility sector's dependence on fossil fuels. The effectiveness of the EV's performance is dependent on the success on how the thermal management systems are designed to make its operating conditions work near the optimal ones. With that, one can increase the lifespan of the battery, avoiding situations of thermal runaway, i.e, preventing situations that lead to the condition of irreversible thermal ignition in the battery pack.

This work can be treated as a case study for the formula student team of Università di Parma, where it is proposed the formulation of a computational model that estimates the heat power dissipated in a lithium ion cell. Using this model one is able to simulate the temperature behaviour during the endurance race of formula student competition. Using the case of the heat transfer in tube banks, it was programmed the model in Engineering Equation Software (EES) and compared the temperature evolution with Ansys Fluent software and the real temperature tracked by NTC thermistors in the battery case.

The results shown that it is possible to validate the final temperature, where one achieve 7.01% and 6.03% of relative error, when applying EES and Ansys Fluent models, respectively. Despite the higher error of EES, the model itself makes a better prediction of the maximum cell temperature evolution than the Ansys model. The methodology was applied to LG, Molicel and Melasta cells, being possible to achieve a lower maximum temperatures than using the LG cells. In what concerns the maximum temperature difference in the battery's module, the value of 3.96ºC was obtained for the Molicel cells at low speed, being under the 5ºC suggested by the literature. The Melasta cell's model shows that for high and medium speeds is still possible to be close to the 40ºC limit of maximum temperature, also recommended by literature. However, it is achieved a 7.64ºC for maximum temperature gradient in high speed for the pouch cells. Although not being critical, the results suggests that some optimizations to the cooling system should be considered.

Finally, one concludes with new approaches to refine the model, e.g., tuning the model to make the input parameters of heat generation and velocity closer to reality. Also, for this case study, if one wishes to keep the actual cooling system and value more the stabilized functioning of the cells, the Molicel cells are a good fit. On the other hand, if high power and capacity are more desired, at the expense of a slight reduction in the electric transmission efficiency in the battery pack, the Melasta cells can be the solution.

Keywords: Lithium-ion cells, Formula SAE, Air-cooling systems

Resumo

O grande investimento na indústria dos veículos elétricos (VE) tem sido acelerada pela: procura da redução das emissões de gases com efeito de estufa; e pelos objetivos estabelecidos no COP28 para reduzir a dependência nos combustíveis fósseis no setor da mobilidade. A eficácia do desempenho dos VE depende do sucesso de como os sistemas de gestão térmica são projetados para que as suas condições de funcionamento operem próximas das ideais. Com isso, é possível aumentar a vida útil da bateria, evitando situações de "thermal runaway", ou seja, precavendo cenários que conduzam à situações irreversíveis de ignição térmica no conjunto de baterias.

Este trabalho pode ser tratado como um caso de estudo para a equipa de formula student da Università di Parma, onde se propõe a formulação de um modelo computacional que estima a potência calorífica dissipada numa célula de iões de lítio. Utilizando este modelo, é possível simular o comportamento da temperatura durante a corrida de "endurance" da competição de formula student. Usando as formulações dos modelos da transferência de calor em "tube banks", foi possível programar o modelo no Engineering Equation Software (EES) e comparar a evolução da temperatura com o software Ansys Fluent e a temperatura real registada por termístores NTC situados no módulo da bateria.

Os resultados mostraram que é possível validar a temperatura final, atingindo-se 7,01% e 6,03% de erro relativo aplicando os modelos em EES e Ansys Fluent, respetivamente. Apesar do erro mais elevado no EES, o modelo faz uma melhor previsão da evolução da temperatura máxima da célula do que o Ansys. A metodologia foi aplicada para as células LG, Molicel e Melasta sendo possível atingir temperaturas máximas mais baixas do que as que se obtiveram com as células LG. No que diz respeito à diferença máxima de temperatura no módulo da bateria, obteve-se o valor de 3,96ºC para células Molicel à velocidade mais baixa, ficando abaixo dos 5ºC sugeridos pela literatura. O modelo com a células Melasta mostra que, para velocidades altas e médias, ainda é possível estar próximo do limite de 40ºC de temperatura máxima, também recomendado pela literatura. No entanto, é obtido um gradiente de temperatura máxima de 7,64ºC a alta velocidade para as células do tipo "pouch". Embora não seja crítico, os resultados sugerem que devem ser consideradas algumas otimizações ao sistema de arrefecimento.

Finalmente, conclui-se com novas abordagens para refinar o modelo, por exemplo, ajustando o modelo para que os parâmetros de entrada de produção de calor e velocidade estejam mais próximos da realidade. Além disso, para este caso de estudo, se existir o desejo de se manter o sistema de arrefecimento atual e se valorizar mais o funcionamento estável das células de lítio, as células Molicel são uma boa opção. Por outro lado, se forem desejadas maiores potências e capacidade, ao custo de uma ligeira redução da eficiência de transmissão elétrica no conjunto de baterias, as células Melasta podem ser a solução.

Keywords: Células de iões de lítio, Formula SAE, Sistemas de arrefecimento a ar

Acknowledgments

I would like to express my gratitude to all the people involved in this wonderful academic journey, since the first day until this moment. Here I had the opportunity to learn about the beauty of the engineering, make friends, share lifelong experiences and develop my character as a person.

First to my parents, who have always motivated and encouraged me to follow my dreams, being the two figures that I appreciate having in my life to share my losses and successes. Additionally, I extend my thanks to my family members who shared their unconditional love wishing me the best.

A special reference to my girlfriend Alexandra, the person who gave a special shine to my days in this journey, motivated me to do my best and always asked me to explain this work to her.

To my old friends with whom I shared my dreams way time before college and are still here giving their support. To my college friends who I recently got along with, but were the ones that shared beautiful moments of friendship with me and shaped my character. Specially to Nuno Machado, who also did his work at UNIPR, gave me his friendly advice throughout these months and made the experience of living in Italy more enjoyable and fun.

I would like also to appreciate the guidance and support of my Professor and supervisor Eliseu Monteiro at FEUP, for all the lessons and valuable insights that enriched the quality of this work.

A special mention to Professor Fabio Bozzoli at UNIPR, who made possible the development of this work, who advised me and offered to me his expertise. Also to Professor Alessandro Soldati whose knowledge in electronic power systems helped me to clarify some new concepts.

Not forgetting my friends at UNIPR Racing Team, who welcomed me with open arms and made me feel at home and part of this incredible team. Specially to Manlio Maghenzani who gave me support and clarified my doubts during the development of this work.

To all of you, thank you.

Pedro Ramos

"Perfer et obdura – dolor hic tibi proderit olim"

Ovidius

Contents

List of Figures

List of Tables

Nomenclature and Abbreviations

Roman Symbols

S_t	Distance between Cells' centers	[m]
D	Diameter of the Cell	[m]
L	Length of the Cell	[m]
a_T	Cell Spacing	[m]
A_s	Surface Area	[m^2]
N_T	Number of Cells in Parallel	[-]
N	Number of Cells	[-]
m	Mass	[kg]
m_{cell}	Cell's Mass	[kg]
$\dot{m}$	Air Mass Flow Rate	[kg/s]
V	Air Velocity	[m/s]
V_{max}	Max Air Velocity	[m/s]
$R_{int,i}$	Internal Resistance at discharging current i	[Ω]
U_{ref}	Reference discharging Voltage	[V]
U_i	Voltage at discharging Current i	[V]
I_{ref}	Reference discharging Current	[A]
I_i	Discharging Current i	[A]
T	Ambient Temperature	[°C]
t_m	Air Mean Temperature	[°C]
t_e	Air Exit Temperature	[°C]
t_i	Air Inlet Temperature	[°C]
t_s	Cell's Surface Temperature	[°C]
h	Convection Heat Transfer Coefficient	[W/(m^2·K)]
c_p	Specific Heat	[J/(kg·K)]
k	Thermal Conductivity	[W/(m·K)]
ΔT_{lm}	Logarithmic Mean Temperature Difference	[ºC]
R_e	Reynolds Number	[-]
Nu	Nusselt Number	[-]
P_r	Prandtl Number	[-]
$P_{r,sup}$	Prandtl at t_s	[-]
$\dot{Q}_i$	Total Heat Flux at discharging Current i	[W]
$\dot{Q}_{irr,i}$	Irreversible Heat Flux at discharging Current i	[W]
$\dot{Q}_{rev,i}$	Reversible Heat Flux at discharging Current i	[W]
$\dot{Q}_{air}$	Heat Flux transferred to air	[W]
$\dot{Q}_{cell}$	Mean Heat Flux dissipated by each cell	[W]

Greek Symbols

ρ	Density	[kg/m^3]
μ	Dynamic Viscosity	$[Pa \cdot s]$

Acronyms

CFD	Computational Fluid Dynamics
COP	Conference of the Parties
DOD	Depth of Discharge
GHG	Greenhouse Gases
HP	Heat Pipes
IEA	International Energy Agency
NTC	Negative Temperature Coefficient
NTGK	Newman, Tiedemann, Gu, and Kim Model
PA	Pure Paraffin
PCM	Phase Change Materials
PHP	Pulsating Heat Pipes
PTC	Positive Temperature Coefficient
SAE	Society of Automotive Engineers
SOC	State of Charge
VCU	Vehicle Central Unit

Chapter 1

Introduction

Concerns about climate change led to a lot of discussions world-wide to decelerate the rhythm of natural catastrophes. Fossil fuel products such as gas, oil and coal represent about 80% of the world's energy production [1] and are pointed out to be the cause of these events. The high level of Green House Gases emissions (GHG) and air pollutants led some countries to provide some solutions to mitigate the problem.

Recently, on 13th December 2023, COP28 took place in Dubai so that nations could strike a deal to transition away from fossil fuels. Nearly 200 representatives of world countries agreed to reduce global consumption of fossil fuels and achieve net zero by 2050, aiming to send a message to policy-makers and investors that the world is cooperating to break with it. Some governments of Europe and from the U.S had the decision of retiring fleets of coal-fired power and had been called out to speed up efforts to invest in the triplication of renewable energy capacity by 2030 [40]. At that point it will be possible to achieve a higher diversification of the energy mix and to achieve a lower dependency in the fossil fuel market and its volatile prices.

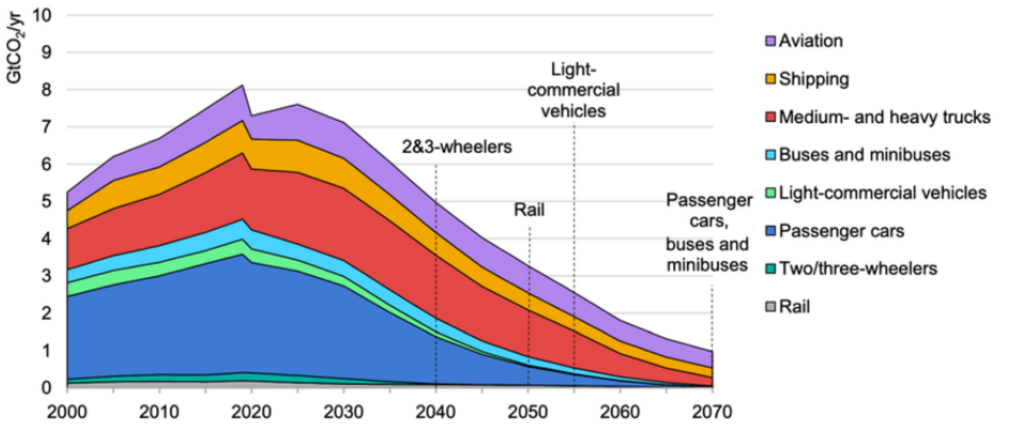

IEA 2020. All rights reserved.

Notes: Dotted lines indicate the year in which various transport modes have largely stopped consuming fossil fuels and hence no longer contribute to direct emissions of CO_2 from fossil fuel combustion. Residual emissions in transport are compensated by negative emissions technologies, such as BECCS and DAC, in the power and other energy transformation sectors.

Figure 1.1: CO_2 current and projected global emissions by sector of transportation [1]

Rapid innovation is urgently needed to deploy new low emissions technologies in areas where it is hard to address, e.g., heavy industry and long-distance transport. Figure 1.1 depicts the current data of CO_2 emissions and what are the projections for the future, till the year of 2070. One of these technologies is the carbon capture used for the preservation of fossil fuels, where its use in North America and Europe constitutes 75% of the global application [1].

The transition to electric mobility of persons and goods is also in scope. Electric vehicles are the key-technology to enhance the decarbonization of road transportation, accounting the cars and light trucks for over 16% of global energy-related emissions. For 2023, it was estimated that almost one in five cars sold would be electric [1]. If the growth experienced in the past two years is sustained, CO2 emissions by 2030 can be put on a pathway aligned with the Net Zero Emissions by 2050 [22].

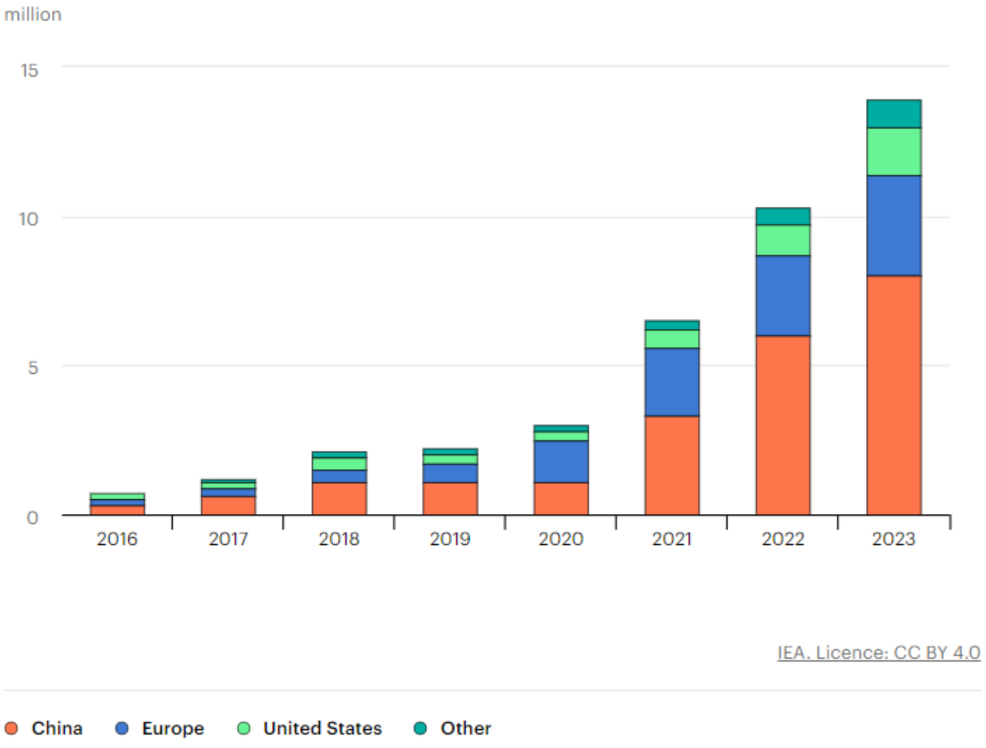

Figure 1.2: Electric car sales, 2016-2030 [1]

The transformation speed is different across different sectors and regions, e.g., the electric cars sales of the market in 2022 in China, U.S. and Europe represents almost 95% [1]. These kind of results are possible nowadays in a few regions where clean technologies are more available and its production costs are dropping rapidly. According to IEA some countries are accomplishing notable progress:

- Norway occupies the leadership in rates of electric vehicle (EV) deployment, accounting for 88% of the share of electric car sales reaching in 2022.

- In 2022, China totalizes nearly 60% of all new electric car registrations of the entire world.
- The European Union implemented new CO2 standards for new cars and vans in March 2023, requiring a reduction of 55% and 50% in emissions, respectively, by 2030 (compared to 2021), and 100% for both by 2035.
- The Inflation Reduction Act (IRA) in the United States has triggered a rush by global electromobility companies to expand their manufacturing operations. From August 2022 to March 2023, prominent electric vehicle (EV) and battery manufacturers collectively disclosed investments totaling USD 52 billion in North American EV supply chains, with approximately 50% allocated to battery manufacturing and around 20% each designated for battery components and EV manufacturing.

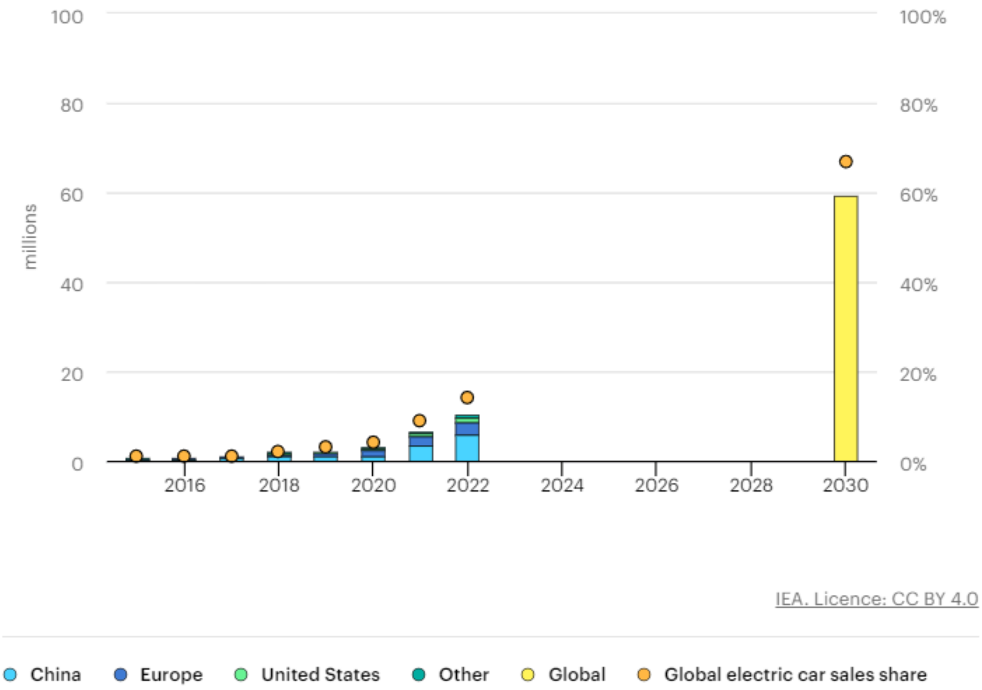

Figure 1.3: Electric car sales and sales share in the Net Zero Scenario, 2015-2030 [1]

However, electric vehicles are not yet a global phenomenon. Sales in developing and emerging economies have been slow due to the relatively high purchase price of an electric vehicle and a lack of charging infrastructure availability. Most charging demand is currently met by home charging. Public chargers are needed to provide the same level of convenience and accessibility as for refueling conventional vehicles. By 2030, the net zero scenario predicts the installation of 17 million public available stations, which would entail an increase over the 900k annual additions witnessed in 2022.

1.1 Battery Sensitivity

Currently, the design lifetime of a battery pack is generally around 8 years, or approximately 100,000 miles. However, sometimes, in moderate climate conditions, these batteries can last up to 15 years. The batteries are built with diverse technologies using different compounds, e.g., nickel-metal hydride, lead-acid, lithium-ion and solid-state batteries. The last ones still being researched as they are recently developed. It is expected to reduce with solid-state batteries the carbon footprint of EV batteries by 40% and to enhance its autonomy providing a 500 miles range of driving capacity [30].

The lithium-ion batteries are the most used today in EVs. Compared to the other compounds, they present a higher power-to-weight and power-to-energy ratios. Their capacity to be recycled and to work with excellent high-temperature performance make them an attractive choice for its use.

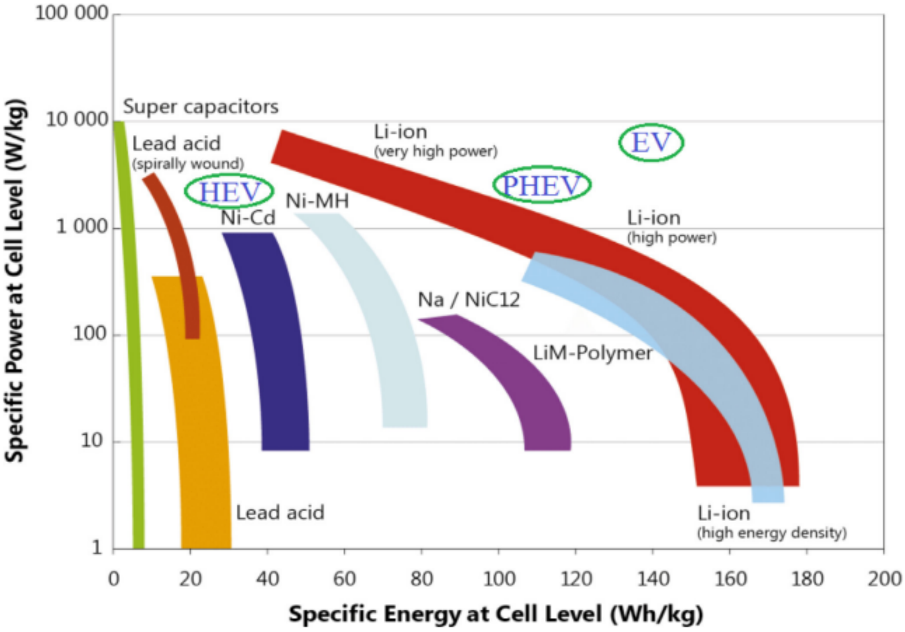

Figure 1.4: Power-to-Energy vs Power-to-Weight ratios of various electrochemical batteries [3]

For producers and consumers, the safety of the EVs is the number one concern among other aspects. The Li-ion cells are made of organic volatile solvents like ethyl methyl carbonate as electrolyte [3], which need a special attention to avoid thermal runaway (TR) situations, i.e., a process in which the internal heat generated is more than the heat dissipated by the battery, what leads to its own destruction [20].

The Li-ion batteries present some problems dealing with extreme temperatures, they are very sensible in what gives concern to the loss of power and energy in charge/discharge cycles. This problem can develop on very hot days and in sub-zero temperatures. The last scenario is common in Canada, some north European countries, and Russia for example, and it can degenerate in 40% the battery power and energy potential because of the loss on ionic conductivity at low temperature.

Below 5ºC the regenerative breaking technology starts to become non-effective for different states of charging (SoC), as studied in Tripathy et al. (2016), and below -15ºC the cell is not able to meet its charging power requirements for any driving-cycle.

For the US06 test pattern defined by EPA (U.S. Environmental Protection Agency), which considers aggressive driving conditions with frequent accelerations/decelerations and high speeds, the cell could not discharge the desired power below -22.5ºC for 75% SOC [2, 38]. Thermal Management systems also take into count this problem, it is needed a pre-heat of the battery pack to enhance the battery's performance, however, the use of rapid heat up phase (15min) can lead to its drainage [22]. Acknowledging those facts it is important to find a sweet spot between the performance of the battery's discharge ability and the potential loss of charge in it.

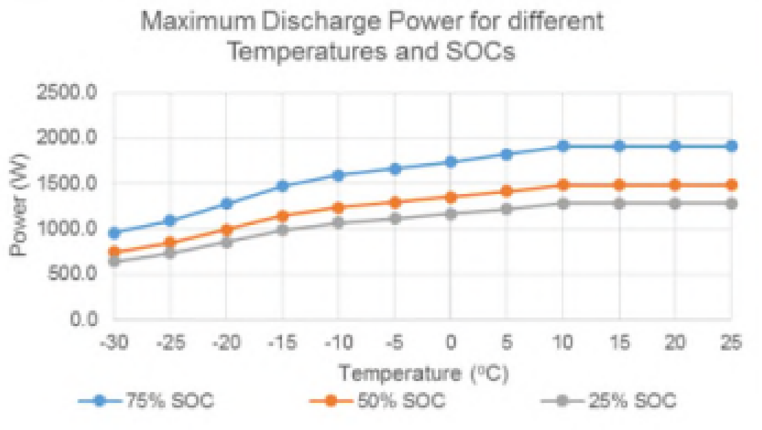

Figure 1.5: Maximum Discharge Power displayed by the cell at different SOCs and Temperatures [38]

As sentenced previously, the behavior of the batteries in hot climatic conditions must be studied. The optimal temperature range is around 15-35ºC [22], or for other authors 20-40ºC [16], and when the temperature is higher the charging storage start to decrease as a consequence of the modification of the surface coatings on the electrodes and phase changes of the lithium electrode [21]. A substantial increase in the battery temperature give rise to the acceleration of electrolyte reduction reactions (160-170ºC), where an additional heating prompts TR with inflammation or even explosion in a worst-case scenario [3]. Furthermore, the maximum temperature difference of 5ºC in the hole battery should also be considered to ensure an equal load distribution over its cells, otherwise some of them will deteriorate first and compromise the normal operation of the battery pack [47]. Therefore, thermal management systems represent also an important role to increase battery lifetime prevent early cost replacement, rapid temperature rise that lead to loss of efficiency in charging/discharging cycles and TR with refrigeration and venting systems that are presented more upfront.

1.2 The UNIPR Racing Team

The Formula Student began in 1982 under the organization of SAE (Society of Automotive Engineers). The first edition was disputed by four teams from the United States of America, in a dynamic contest. Only in 1998 the competition gives its first steps in Europe, being in 2005 the year when it realizes the first Formula SAE Italy event, organized by ATA (Associazione Tecnica dell'Autoveiculo) [34]. After two years the UNIPR Racing Team was founded. The group was formed by mechanical engineering students who in the same year participated on the Fiorano circuit in class 3 category (engineering project contest), conquering a place at the podium among the best projects [39].

In 2008/2009 the team competed in CV category with the PR02B vehicle, which was constructed in sandwich panels of carbon fiber, a honeycomb in aluminum alloy and 4 straight cylinder motor Susuki GSX-R 1997 with 600cm^3 [34].

Figure 1.6: PR02B model of UNIPR Racing Team (up) and last EV model (down) [34, 39]

After some successes, the team engaged in the following events achieving great results in Hungary, Czeck Republic and Italy. In 2018, a new adventure was on the way. It was designed the first prototype to compete in the Electric Vehicle category, which was the prototype that won the 2^{nd} place in design contest.

More developments were made throughout the years with an increase in the number of team members and sponsors' contributions. UNIPR Racing Team is at present time putting efforts for the following two seasons, 2023/2024 and 2024/2025, releasing a new-innovative and ambitious project of its first Autonomous Driving Car [39].

The development of this Master's Dissertation was made in the "Reparto Aerodinamica e Raffreddamento", where CFD simulations, design and sizing of cooling systems are carried out. In the presence of the high voltage battery (600 V), the team is concerned about the maintenance of the optimum range of temperatures to ensure a higher performance of the motors, inverters and transmission.

1.3 Objectives

In this work one is focused in comprehend how do the different types of lithium ion cells behave accordingly to the power demand during an endurance race. With that it is intended to develop a model that, in function of the voltage variation with capacity displayed by each cell, allows to estimate the heat power loss.

Having the description of the heat generation, it is pretended to compare the two approaches in terms of accuracy of the results obtained through time with the data collected by the vehicle's sensors. One of the models is based in heat transfer correlations and solved iteratively in EES and the other is solved by using CFD calculations in Ansys Fluent.

Finally, after making conclusions about the validity of the model, one will apply it to the new lithium-ion cells in study and make judgments about their potential implementation in the following seasons of Formula SAE competitions.

1.4 Structure

This work is developed to be easily understood, presenting reasonable detail and being complemented with tables and figures that support all the text.

In Chapter 2 there are reviewed some concepts related to the electric assembly of cells, the type of cells present in the market, some regulations of the Formula SAE competition and a resume of the most common cooling systems used in thermal management of electric vehicles.

Chapter 3 presents the methodology adopted in this work, being explained in detail some procedures and assumptions that will conduct to the results obtained.

Chapter 4 resumes the results obtained and objectively analyses them, in order to understand the impact of the assumptions made.

At the end, in Chapter 5, one conclude about the work proposed and the benefits that can be extracted from it, where there are also referred some interesting improvements to this model in future works.

Chapter 2

Bibliographic Review

In this bibliographic review it is going to be presented some common geometries produced in the industry of lithium ion cells, the technical characteristics of the proposed cells to be used in the next battery pack of UNIPR Racing Team and the type of assemblies that can be adopted to provide the required amount of power by the motors and that are aligned with the Formula SAE regulations. More also, some cooling systems studied among the researchers are presented, using air, liquid cooling and pulsating heat pipes.

2.1 Cell Geometry

Lithium ion batteries are presented in different applications with diverse cell's format according to the needs of its users. It is possible to find in the market cylindrical, prismatic and pouch lithium cells as one can see in the following Figure 2.1.

Figure 2.1: Different lithium ion cells format [32]

2.1.0.1 Cylindrical Cells

Cylindrical cell is the type of model that is produced in mass world-wide. It consists in sheets of battery anodes and cathodes that are rolled up and packed into a cylindrical-shaped containers. These kind of cells can be connected to other cells using busbars by welding its connectors in order to increase the battery voltage or capacity. One can find these cells in lamps, toys and portable devices.

It presents some advantages as being more suitable to be thermally managed as the space between cells allows the working fluid to circulate and dissipate the heat generated. As far what concerns mechanical stability, the cylindrical shape provides a good pressure distribution during high charging/discharging rates. In the other hand, high capacity batteries with large amounts of cylindrical cell modules require a complex connectors system which will, at the end, enlarge the battery weight [32].

2.1.1 Prismatic Geometry

This type of cell is composed by great amounts of anodes, cathodes and ceramic separators sandwiched to fit in a cubic case made of hard plastics or sometimes in metal. The mentioned structure is projected to avoid the swelling of its cells and to provide higher nominal capacity and overall energy density.

Comparing to cylindrical cells, these ones are lighter because it is optimized the battery pack's space compartment but at the same time it presents more expensive production costs and higher potential stress for the electrodes and separators more close to the case's corners. One can find prismatic geometries in electric vehicles, grid energy storage and in some medical fields [32].

2.1.2 Pouch Cells

On the contrary of the other type of cells, the Pouch cells do not have a rigid outside case. The electrode and separator layers of the pouch are stacked and there is a special care dealing with them as they need enough space as they display some tendency to swell.

A battery can use this kind of cells by connecting large amounts of pouch cells with tabs and busbars. It has its advantages as it is the most light and flexible solution for battery packs, however one must take into attention the exposure to external impacts or punctures, needing to be well encapsulated. This solution is not very suitable to industry because of the reasons mentioned above, but it has its application linked to the electronics of smartphones, drones, laptops and wearable devices [32].

2.2 Cells Characteristics

In this work there were considered the following models of lithium-ion cells presented in Figure 2.2. One of them is the model INR-21700-P42A from Molicel, a lithium nickel manganese cobalt oxide cell with a capacity of 4200 mAh, and the other a Lithium-Polymer (LIP) pouch cell from Melasta with 6600 mAh of capacity.

Figure 2.2: On the left is presented the INR-21700-P42A from Molicel and on the right the LIP pouch cell from Melasta. Source: *Molicel and Melasta*.

2.2.1 Molicel INR-21700-P42A

In Table 2.1 it is presented some technical data regarding the refered cylindrical cell and in Figure 2.3 is presented the discharge rate characteristics of the cell, where one can denote how does the cell voltage evolves with cell capacity for specific discharge currents.

Table 2.1: Molicel INR-21700-P42A characteristics [29]

Capacity	Typical	4200 mAh
		15.5 Wh
	Minimum	4000 mAh
		14.7 Wh
Cell Voltage	Nominal	3.6 V
	Charge	4.2 V
	Discharge	2.5 V
Charge Current	Standard	4.2 A
Charge Time	Standard	1.5 hr
Discharge Current	Continuous	45 A
Typical Impedance	AC (1KHz)	10 mΩ
	DC (10A/1s)	16 mΩ
Temperature	Charge	0°C to 60°C
	Discharge	-40°C to 60°C
Energy Density	Volumetric	615 Wh/l
	Gravimetric	230 Wh/kg

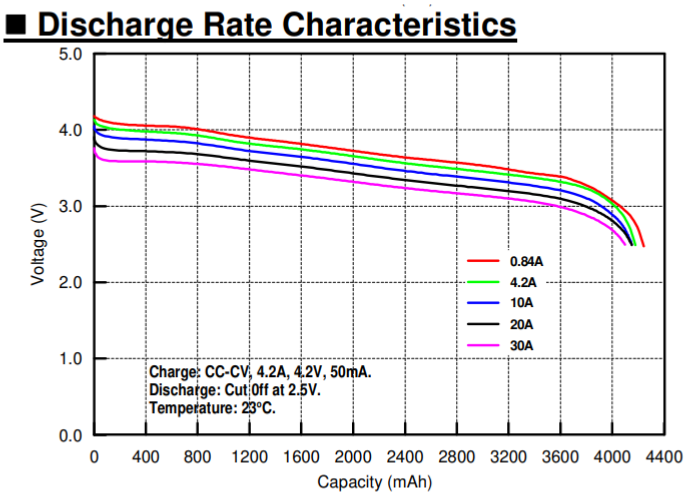

Figure 2.3: Discharging characteristics at different discharging currents [29]

2.2.2 Melasta SLPBB042126

As it was done for the previous cell, in this subsection in Table 2.2 it is presented the technical data of the pouch cell and in Figure 2.4 is depicted the discharge rate characteristics of the cell, where the cell voltage evolves with cell Depth of Discharge (DoD) for specific discharge currents. From Equation 2.1 its defined the way DoD is calculated, as quotient between the current and nominal cell capacities. Also in Equation 2.2 is presented the relation between DoD and the SOC, which means the remaining energy available in the cell.

Table 2.2: Melasta SLPBB042126 characteristics [27]

Capacity	Typical	6850 mAh
	Minimum	6600 mAh
Cell Voltage	Nominal	3.7 V
	Charge	4.2 V
	Discharge	3.0 V
Charge Current	Standard	13.2 A
Discharge Current	Continuous	99 A
Typical Impedance	AC (1KHz)	2 mΩ
Temperature	Charge	0ºC to 45ºC
	Discharge	-20ºC to 60ºC

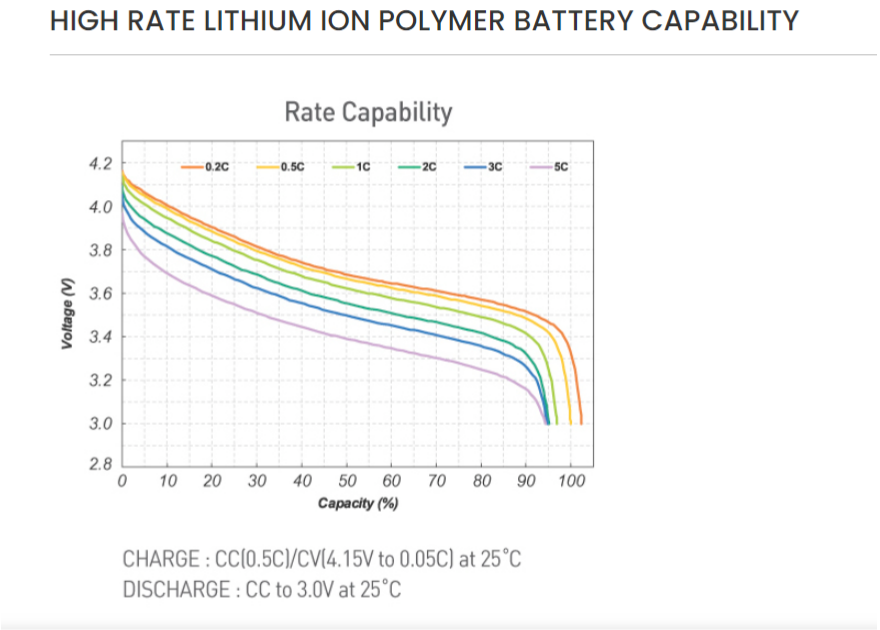

Figure 2.4: Discharging characteristics at different discharging currents [4]

$$DoD(\%) = \frac{Actual\ Capacity}{Nominal\ Capacity} \times 100 \tag{2.1}$$

$$SoC(\%) = 100 - DoD(\%) \tag{2.2}$$

2.2.3 LG 18650HE2

Although it was not referred before as a cell to be evaluated in this study, the fact is that this model from LG has a significant role because this cells were used in season 2022/2023. As it is going to be shown in the following chapters, the tracked data of the current used during the competition was obtained for this cylindrical cells and allowed to develop a model to predict power dissipation for new cells for the following seasons. In Table 2.3 are summarized the characteristics of the LG 18650H2 cell and in Figure 2.5 the respective discharge pattern obtained from [24].

Table 2.3: LG 18650HE2 characteristics [5]

Capacity	Nominal	2500 mAh
Cell Voltage	Nominal	3.60 V
	Charge	4.2 V
	End voltage (cut off)	2.5 V
Charge Current	Standard	1250 mA
Discharge Current	Continuous	500 mA
Typical Impedance	AC (1KHz)	20 mΩ
Temperature	Charge	0°C to 50°C
	Discharge	-20°C to 75°C

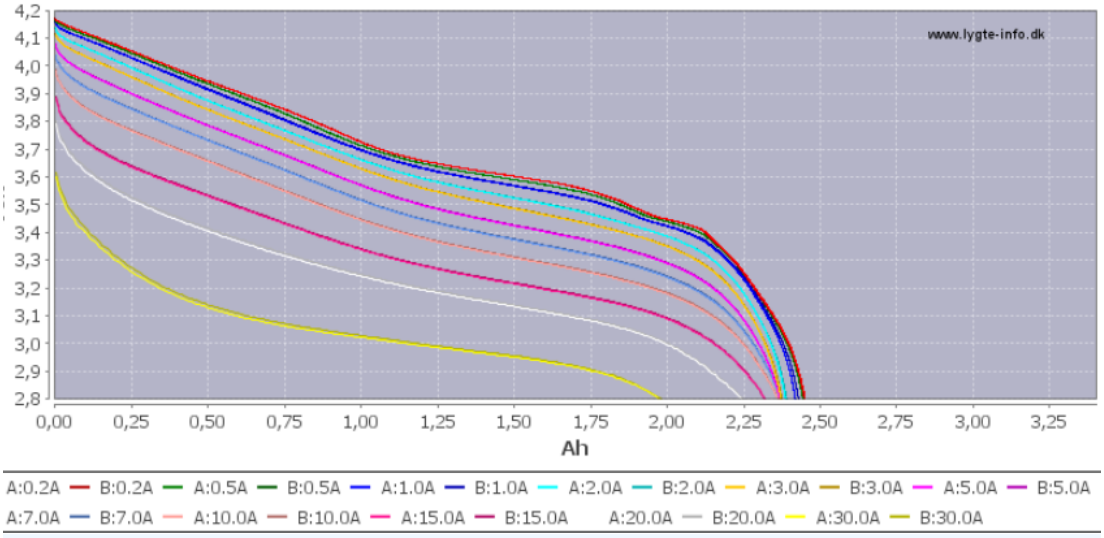

Figure 2.5: Discharging characteristics of LG at different discharging currents [24]

2.3 Battery Modules

When assembling the cells into modules and then the modules to form the battery pack, the way its cells are connected are essential for the battery overall performance. Getting to know the driving requirements during a Formula Student competition is a essential step to define some parameters that have to be fulfilled, e.g., the battery voltage, total capacity, energy displayed.

There are two basic ways of connecting cells, doing the parallel or the series assembly. In Figure 3.10 is shown a scheme of the mentioned basic connections and what is the resulting voltage and current in each situation.

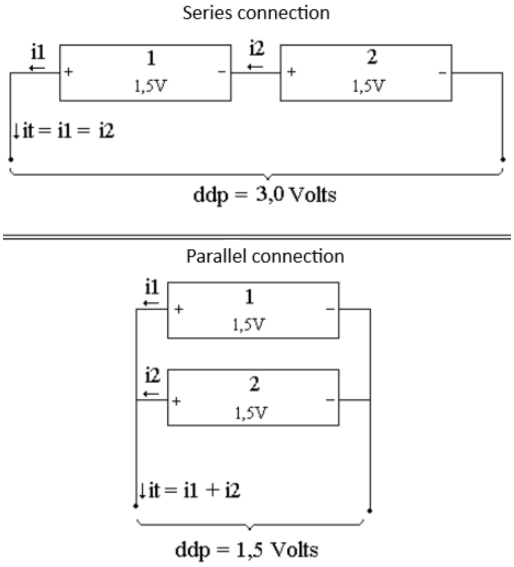

Figure 2.6: Series and Parallel connections between cells adapted from [7]

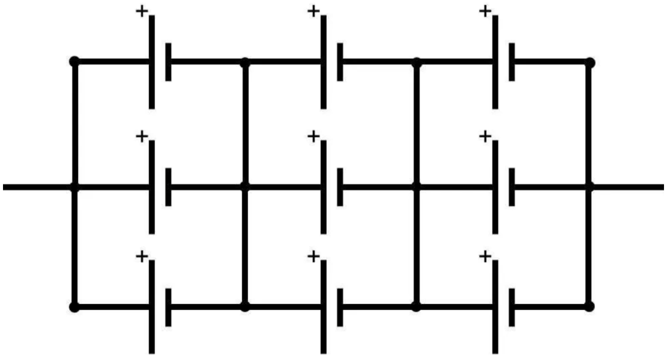

Figure 2.7: 3P3S cell assembly scheme [9]

In Figure 2.7 one can visualize an example of a 3P3S cell assembly where there is a pattern of three cells connected in parallel that repeats in series three times. As an example, if each cell has a nominal voltage of 1.5V and a discharge current of 2A, the hole module is going to display at the end a voltage of 4.5V (1.5 x 3 series) and a current of 6A (2 x 3 parallels).

In what gives concern to the cells in study, the formula SAE competition established in the regulations, in [19], that the maximum power measured by the Energy Meter can't exceed 80kW and the maximum allowed voltage that can occur between two points must not exceed 600V DC. Considering the regulations the electronic department established the amount of parallel and series assemblies for each case, where in Tables 2.4 , 2.5 and 2.6 are resumed all the details including the resulting voltage, maximum capacity and current available and also power supplied.

Table 2.4: Battery Characteristics using LG 18650HE2

Name:	Module:	Parameter:	Value:
LG 18650HE2	4P28S	Vn	3.6 V
		I	20 A
		Cn	2500 mAh
		Nr. Modules	5
		Voltage	504 V
		Current	80 A
		Capacity	10 Ah
		Power	40.32 kW

As presented in Table 2.6, the value of the power displayed by the proposed cells exceeds the maximum 80kW allowed by the regulations. The value is a result of the big current discharge that the cell itself dispose. The note in the table indicates that the real value is going to be in consonance with the regulations, where there is already produced coding ,by the software department, which bounds the discharge utilization, i.e., the current use is limited.

Table 2.5: Battery Characteristics using Molicel INR-21700-P42A

Name:	Module:	Parameter:	Value:
Molicel INR-21700-P42A	3P12S	Vn	3.6 V
		I	45 A
		Cn	4200 mAh
		Nr. Modules	12
		Voltage	518.4 V
		Current	135 A
		Capacity	12.6 Ah
		Power	69.984 kW

Table 2.6: Battery Characteristics using Melasta SLPBB042126

Name:	Module:	Parameter:	Value:
Melasta SLPBB042126	2P18S	Vn	3.7 V
		I	99 A
		Cn	6600 mAh
		Nr. Modules	8
		Voltage	532.8 V
		Current	198 A
		Capacity	13.2 Ah
		Power	105.4944 kW (*)

2.4 Other regulations and considerations

In what gives concern to the battery cooling system there's also regulations mentioned in [31], the main ones are:

- Every cooling and lubrication system must be sealed to prevent any type of leakage;
- Every vent for systems containing water must have a collection container with a volume equal to 10% of the total fluid contained in the system or 100 ml, whichever is greater;
- The components of the traction system can only use water or oil as a coolant;
- Temperatures of the battery pack must stay below the maximum temperature recommended by the producer or 60ºC, whichever is the the lowest.

In order to decrease the weight of the battery pack, where are included the Printed Circuit Boards (PCBs), the polymer frames which support the modules and even the cells, air is selected as the cooling fluid due its advantages over the liquid coolant, not needing pipes and pumps.

2.5 Air-cooling systems

For air-cooling systems there are two kinds of strategies, using natural or forced air cooling techniques. The first one relies on natural convection, in which the heat is dissipated due to differences in fluid density without consuming additional power. In the second, the space between cells are useful to allow air movement making use of fans and blowers, which is what characterizes them. The forced air movement among the cells dissipates the heat generated and offer the advantage to preserve and regulate, with high capacity, the optimum working temperature range for its operation in a safety way. However, the use of blowers and fans increase the complexity of the cooling systems and lead to an increase of power consumption, i.e., it affects in a certain way the power that remains available, and the capacity of displaying effectively energy as the battery is used in first instance to provide electrical motion.

The arrangement of the cells impact in the heat dissipation performance of the system. The paper elaborated by T.Hai et al (2022) proposes two different arrangements for the cells in the battery pack, one the aligned layout and the other the unaligned. The study evaluated the effect of each layout in response to a variation of the inlet air velocity for three charging and discharging cycles, where the air inlet was placed at the top of the cells and the outlet at its bottom.

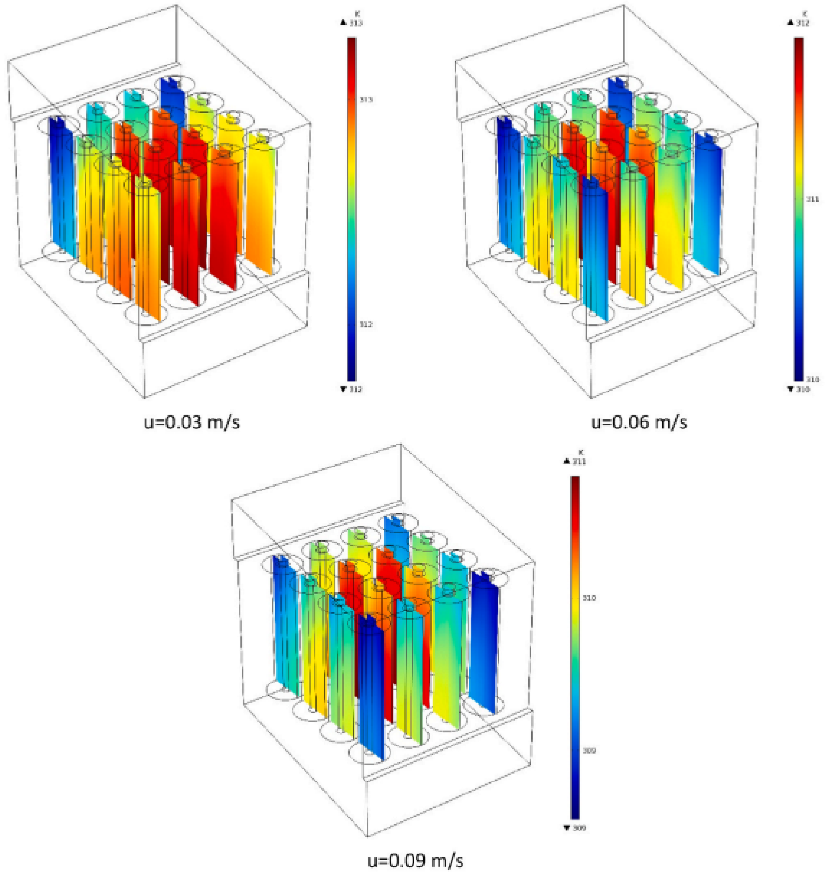

u=0.03 m/s

u=0.06 m/s

u=0.09 m/s

Figure 2.8: Effect of inlet air velocity on the temperature of the longitudinal sections in the aligned layout [15]

Some considerations were done, making use of the NTGK model once the heat generated correlates to the chemical reactions involved between its components. The study came to an end where it was concluded the aligned model ensured better results because the average temperature of the battery pack was lower when there was an increment of the inlet air velocity depicted in the Figure 2.8. It is worth noticing in this work that the battery cells in the center present the highest temperatures in the battery pack as at the same time the ones placed at the corners present the lowest values [15]. Here is notorious the important role of air velocity after three charging cycles on the average and maximum temperature of the battery pack.

Additionally to the air-inlet velocity, some authors such as Jinhong Xie et al (2017) even claim there are other factors which influence the heat dissipation in the battery pack. The mentioned factors are the air-inlet and air-outlet angles as one can see in Figure 2.9. By changing the values of γ and ϕ, with an multi-objective optimization function that maximizes the heat dissipation, the authors found if they were equal to 2.5° and 3°, respectively, the maximum temperature of the battery cells could be lowered by 1.25°C and 0.83°C, maintaining a constant inlet air velocity of 3 m/s [43].

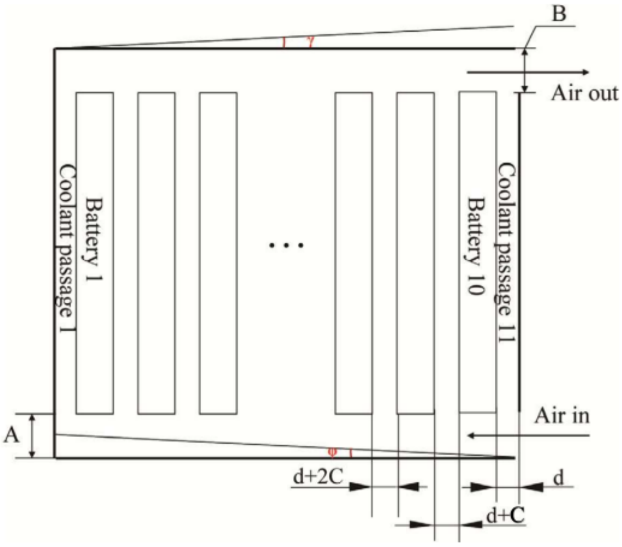

Figure 2.9: Structure of Battery case where A is the height at the end of inlet area, B is the height of the outlet and C is a tolerance value [43]

X.M. Xu et al (2013) considered in his paper the preference for horizontal battery pack instead of the longitudinal one (Figure 2.10) because this type of layout enhances the heat dissipation. The mentioned effect is explained by the shortened airflow path.

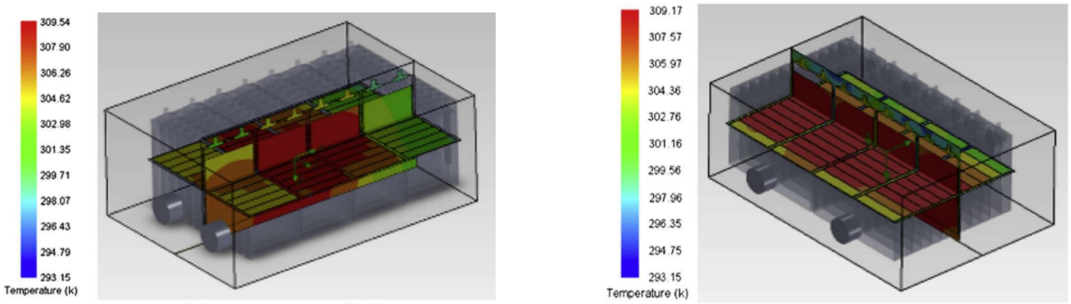

(a) temperature field (a) temperature field

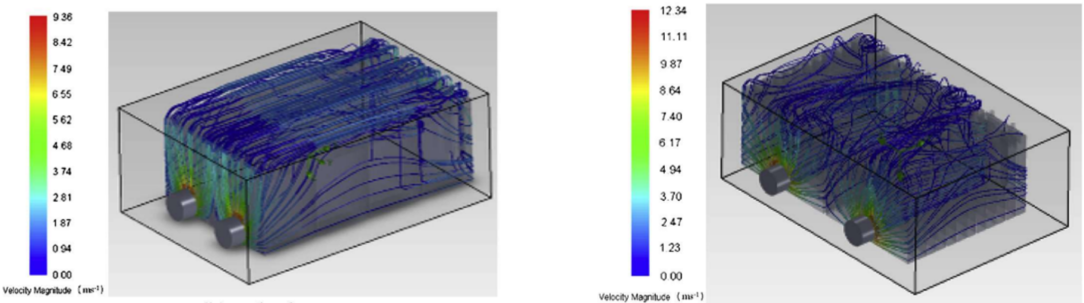

(b) velocity trace (b) velocity trace

Figure 2.10: Temperature and Velocity traces for longitudinal (a) and horizontal (b) battery pack [44]

The airflow in longitudinal battery pack mainly passes on the top of the cells and not through both sides. This behavior doesn't optimize the heat dissipation and that is more notorious when the environmental temperature increases, as the flow rate and average pressure drop between the air inlet and outlet decreases. This scenario is enhanced with the horizontal battery pack as one can compare from the results of the tables below and conclude about its higher cooling capacity. Also, the control volumes located at the central part of the battery pack, more close to the outlet, are the ones presenting the highest temperatures of the module and, on the other hand, the ones at the top close to the inlet present the lowest.

Table 2.7: Data of the heat flow field at different environmental temperatures for the longitudinal battery pack [44]

Environmental temperature (ºC)	20	27	40
Flow rate ($m^3\ \ h^{-1}$)	34.15	33.50	32.21
Maximum temperature rising (ºC)	16.39	13.58	12.01
Maximum temperature difference (ºC)	12.00	9.90	8.69
Average pressure drop (Pa)	76	75	73

Table 2.8: Data of the heat flow field at different environmental temperatures for the horizontal battery pack [44]

Environmental temperature (ºC)	20	27	40
Flow rate ($m^3\ h^{-1}$)	34.77	34.12	32.80
Maximum temperature rising (ºC)	16.02	13.31	11.83
Maximum temperature difference (ºC)	11.05	9.18	8.19
Average pressure drop (Pa)	89	87	84

Some other authors developed new types of apparatus with new working patterns of the cooling system to evaluate the effect it has on energy consumption and cooling efficiency. Fan He et al (2015), projected a case, where 4 cylindrical cells were set up inside of a benchtop wind tunnel equipped with diagnostics and controls instrumentation. The tunnel was equipped with two electric fans with identical power of 0.84 W at the entrance and at the exit as one can see in Figure 2.11. The fans were installed with the purpose to produce reciprocating flow, i.e. they were activated and deactivated alternatively to change the air flow direction.

Also, there were named four working conditions that later in the paper's development presented interesting results which support the use of one of them. There was named the: "HYS+RECP" condition, i.e., the condition with active hysteresis control and reciprocating flow; "NC+RECP", i.e., the condition with no active control and reciprocating flow; "NC+UND", i.e., the strategy with uni-directional air flow with no control; and "NC+NF", i.e., the strategy where there was no air flow (natural convection) [16].

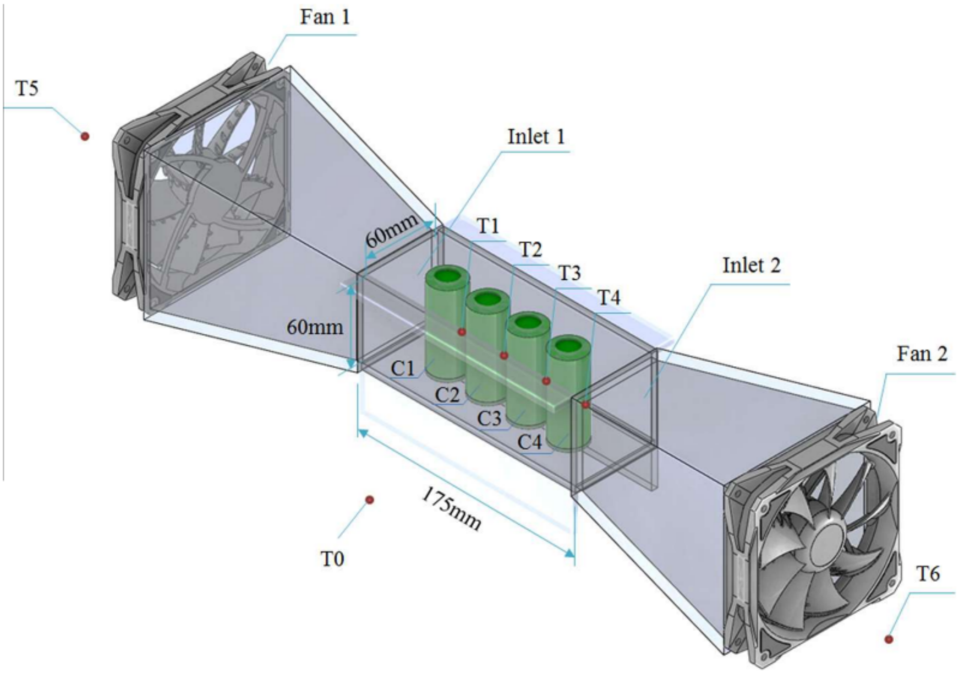

Figure 2.11: Experimental setup depicting the benchtop wind tunnel and the battery module [16]

All the data, e.g., voltage, current and cells temperatures, were tracked by the battery cycler during the charge and discharge cycles. As one can see by the results achieved in Figure 2.12, the alternate flow (NC+RECP) achieves a maximum temperature rise of 4.2ºC and a maximum temperature difference among the four cells of 0.6ºC, while the maximum value of 4.4ºC is achieved by the uni-directional flow (NC+UND) with a 1.3ºC difference between the cells.

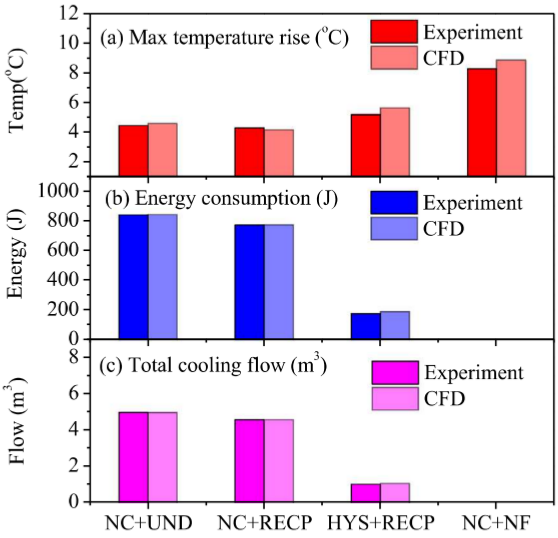

Figure 2.12: Experimental and CFD results for temperature rise, energy consumption and air volume flow rate for different system working conditions[16]

These results show the reciprocating flow enhances the temperature non-uniformity among the cells and, if it has the hysteresis control activated, it is even possible to reduce the air consumption at a the cost of a slight increase on the maximum temperature raise. The data available also shows that "NC+UND" and "NC+RECP" have an higher energy consumption of 820 J compared to 130 J of the "HYS+RECP" strategy. This represents a 84% reduction in "parasitic" energy consumption, as the authors refer, due to the temperature range of the fans activation (active control when temperatures are between 26.5-27.5 ºC) [16].

Rajib Mahamud et al (2011) used a baffle system, i.e., a system with flip door valves as flow distributors to produce a reciprocation flow through the cells in a battery case. The Figure 2.13 depicts how the flip door valves work to orientate the flow. A reciprocation period (τ) was set at 1200 s, in which half of its period the air flows from the left to the right side and the other half from the right to the left side. In the instants when the flow is re-orientated, it only takes a few milliseconds to rapidly become fully developed again.

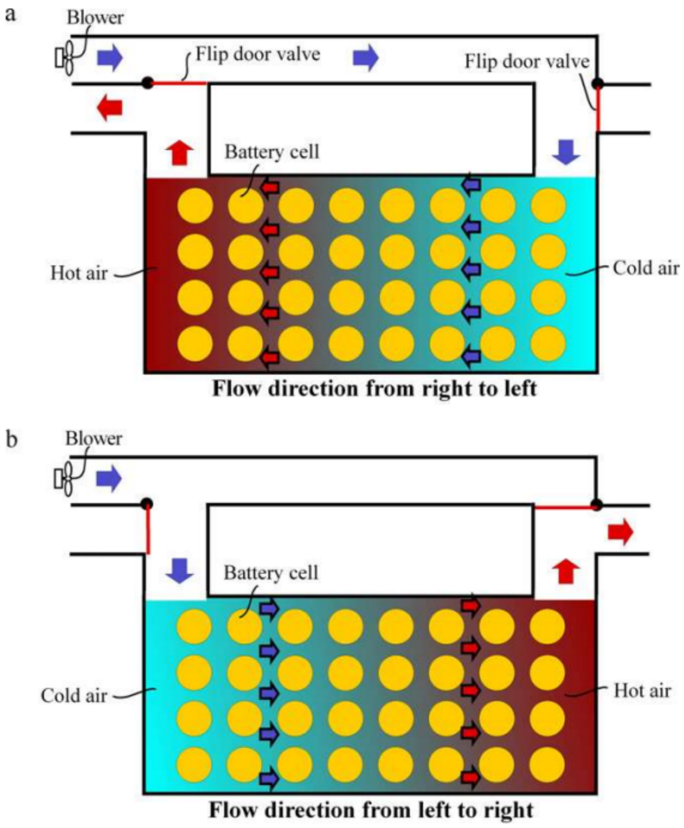

Figure 2.13: Draft of the battery system using flip door valves to create reciprocating flow for battery cooling. In a) The air flows from the right to the left side and in b) from the left to the right side [25]

In the presented study it was taken a representative row of eight cells to evaluate the effects of a few variables on the maximum temperature achieved, maximum temperature difference in flow direction and heat generation. The main variables considered here were the air flow rate and the reciprocation period (τ). In the first one, the maximum temperatures always occur, for different Reynolds number, at the second (2nd) or at the seventh (7th) cells, depending in the flow's direction. The reason why the maximum temperature is not achieved by the last cell is because of its higher exposure to the convective environment due to the bigger re-circulation area formed behind itself [25].

As what matters to the reciprocation periods, the authors tested the effects on the maximum temperature when it reached a quasi steady-state condition by testing the results in a uni-directional flow ($\tau = \infty$) and in a shorter period of time where τ was equal to 120 s, as one can observe in the Figure 2.14.

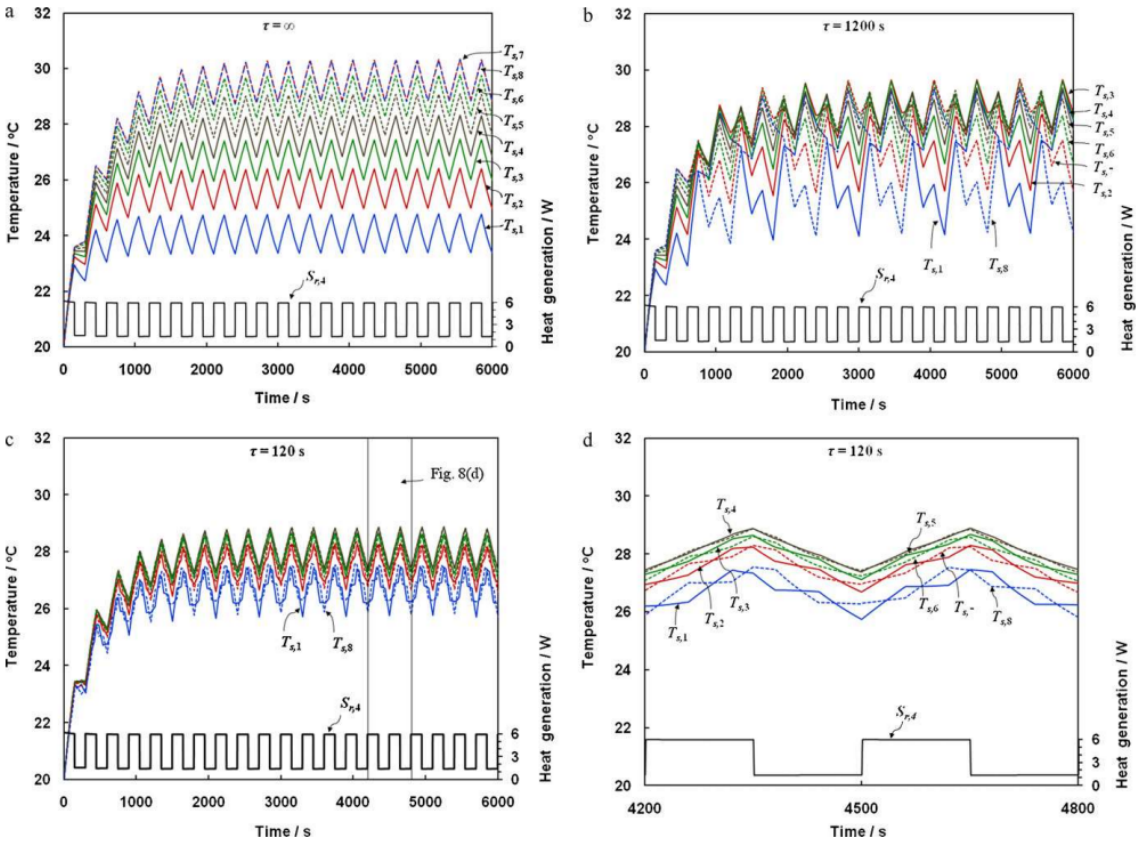

Figure 2.14: Variation of the battery cell temperatures for different reciprocation periods of the battery cell 4 [25]

The previous results were taken for the fourth cell of the row as it is representative of the selected row of cells. It was shown that the shorter the reciprocation period is, the lower the maximum temperature difference of the system and the cell temperature difference. After 5000 s the temperatures and the heat dissipation rates stabilizes, reaching the quasi steady-state condition for all the τ values. It is for τ equals to 120 s that the cell reduces its temperature difference by 4ºC, representing a 72 % reduction when compared with the uni-directional condition, and a maximum temperature decrease of 1.5ºC.

2.6 Liquid-cooling systems

The liquid cooling systems emerge in a way to compensate the drawbacks associated with the use of air-cooling systems. Air-cooling systems are employed in various cooling applications and offer simple ways with its implementation in battery packs, however, the low air conductibility and specific heat may not ensure such effectiveness on keeping an acceptable temperature difference between cells when they work in severe conditions, i.e., working at high discharging rates with high environment temperatures [47].

Liquid cooling systems are divided in direct and indirect applications. The direct systems are distinguished because of the direct contact between the cooling fluid and the battery cells, while the indirect systems involve the use of tubes, heat pipes or cooling plates where the fluid circulates. The first one enhances the cooling performance as there is no additional thermal resistance between the cell and the fluid, moreover [47] refers in its paper if the coolant is flame retardant, it could offer a better fire suppression if anything goes wrong and the battery starts in thermal runaway phenomena. Liquid coolant has its drawback despite the huge advantages: the immersion of the battery pack in coolant increases the weight of the vehicle. That is why the reason of systems that combine liquid and air cooling presented down below.

Luyao Zhao et al (2023) in his paper divided the optimization of the cooling system: 1) Optimization of the liquid cooling regarding the gap spacing between the battery and the cooling jacket, the liquid mass flow rate and number of pipes; 2) By incorporating an auxiliary air-cooling system, it was proceeded an optimization of the orientation of the air flow and air inlet velocity. The design of the cooling jacket is similar to the one which inspired the author from [45] and presented in Figure 2.15.

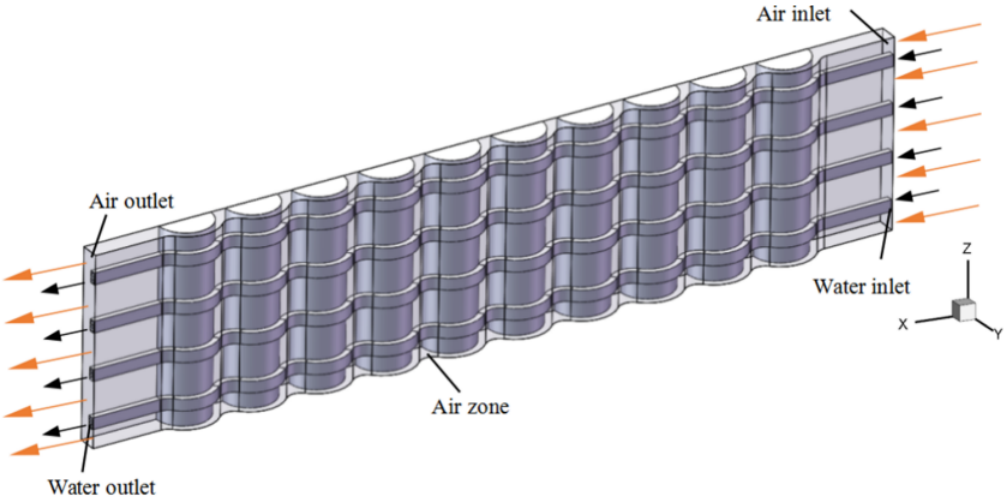

Figure 2.15: Inspiring model for the cooling jacket [45]

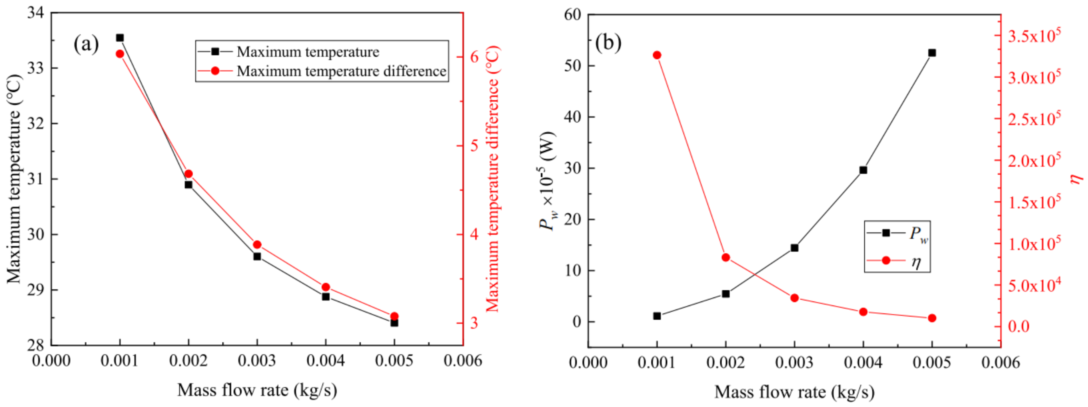

Figure 2.16: Maximum battery temperature and maximum temperature difference (left), power consumption and cooling index (right) varying with mass flow rate [47]

The authors found in a first approach that using a 5mm space gap, the optimal liquid mass flow rate was 0.002 kg/s which states a good balance between the power consumption of the system and an high cooling efficiency that one can conclude from Figure 2.16, resulting in a temperature difference along the battery pack less than 5°C. The two pipeline geometry selection, also ensured a lower temperature difference and lower energy needs when compared to the others pipeline layout. In Figure 2.17 there is a sketch of the cooling jacket and how it is designed to improve the heat dissipation of the cells.

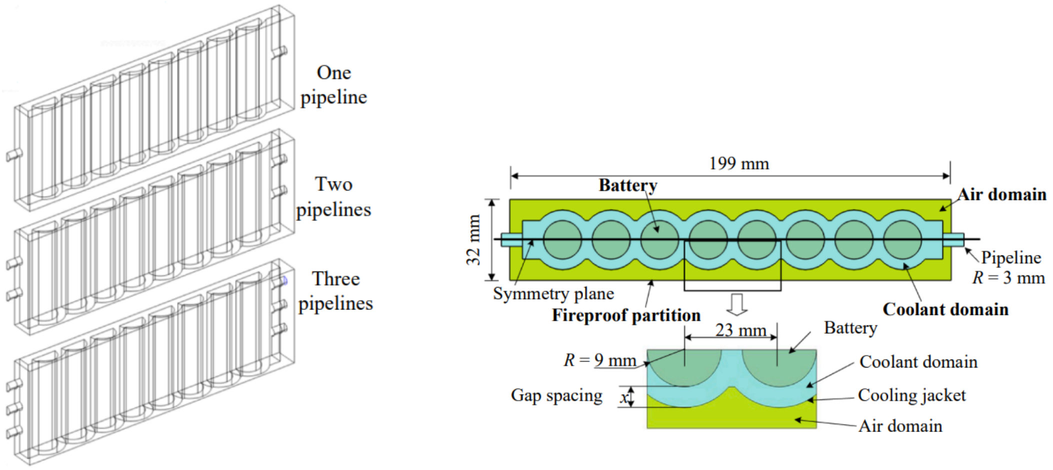

Figure 2.17: On the left are depicted the three studied layouts with different number of air pipelines and on the right a sketch of the cooling jacket [47]

Other authors proposed new concepts using new materials for passive cooling systems, that's the case of PCM (Phase Change Materials) and its subsequent developed versions. PCM materials when absorb heat change their physical state from solid to a biphasic state containing solid and liquid. Using these materials imply taking advantage of its capacity of absorbing latent energy to remove the heat produced by the battery cells. However, as this type of material has lower thermal conductivity, it cannot be used in a continuous mode, i.e., it is not able to meet a long-time heat removal from the modules. Some researchers tested how did the addition of graphene/carbon nanotubes or aluminum foam impacted the surface temperature and uniformity of the modules [18].

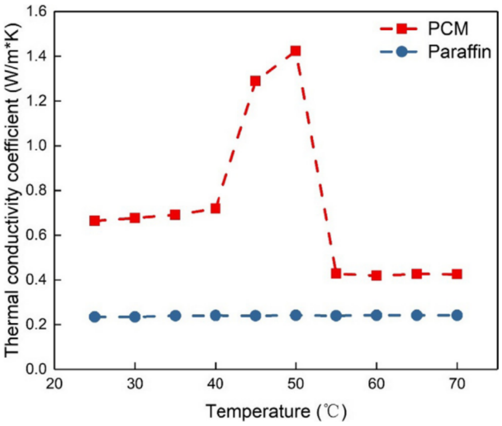

Figure 2.18: Thermal conductivity coefficient varying with temperature [18]

In Figure 2.18, it is possible to notice that at around 45℃ there is an higher increase on the thermal conductivity coefficient accompanied with the bigger temperature rise for the PCM while pure paraffin (PA), one of the components of PCM, remains constant. Despite of the fact that the addition of expanded graphite to the mixture of PA and epoxy improves thermal conductivity of PCM and consequentely the cooling efficiency of the system, significant performance of the modified PCM is not achieved.

Considering this, allying heat pipes to PCM in cooling systems can overcome that drawback and to be found as a viable solution. Heat pipes and plate heat pipes are considered as the most effective passive method of carrying thermal energy. They consist in tubes divided in three sections: Evaporation; Adiabatic; and Condensing sections (Figure 2.19). In its interior circulates a phase-change fluid that when passes through the evaporation section is heated up and transformed in vapor state, carrying the heat to the condenser section where it returns to the liquid sate. After condensing, the liquid comes back to initial section either by gravity or capillarity [37, 18].

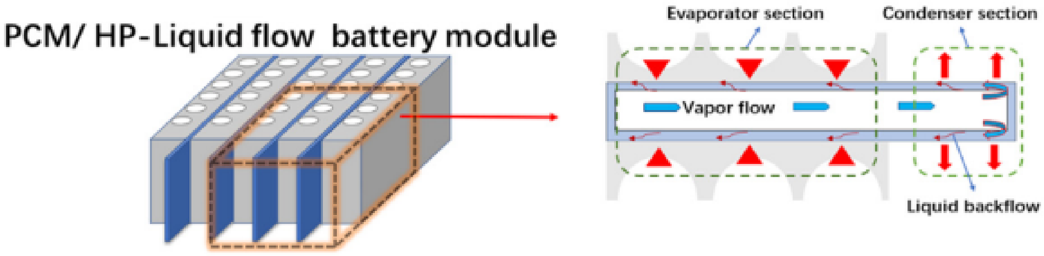

Figure 2.19: Representation of the evaporation, adiabatic and condensing sections of a heat pipe [18]

Qiqiu Huang et al (2018) in his paper tested three cooling methods to conclude what would be the best option to be implemented: heat pipes filled with air (HP-Air) or filled with ethyl alcohol (HP-Liquid) assisted with PCM. In the experiments the battery cells were charged at 1C and discharged from 1 to 3C. The results were compared with the reference for the results, the system which only used PCM with no heat pipes.

Figure 2.20 a) shows that at 1C the PCM remains in solid state, without occurring any phase change, denoting that at this discharge rate conduction is the only heat transfer phenomenon. Also, for 2.20 b) and c), comparing different cycles, the system PCM/HP-Liquid improved the performance, increasing the transferring heat capacity of the heat pipes that was added to the latent heat transfer. During the experiment process, the PCM/HP-Liquid exhibits a stable and similar temperature profile after the initial cycles, what does not denotes when it is used the other two models.

Thus, it is noticeable from the graphs that the amount of heat generated by the cells cannot be handled by the amount of energy that can be absorbed in the pure PCM layout, i.e., the heat transfer speed to the outside air is very low when compared with the velocity of the heat absorbed by it. This is the reason PCM alone don't fit with long continuous applications, specially at considerable energy demands [18].

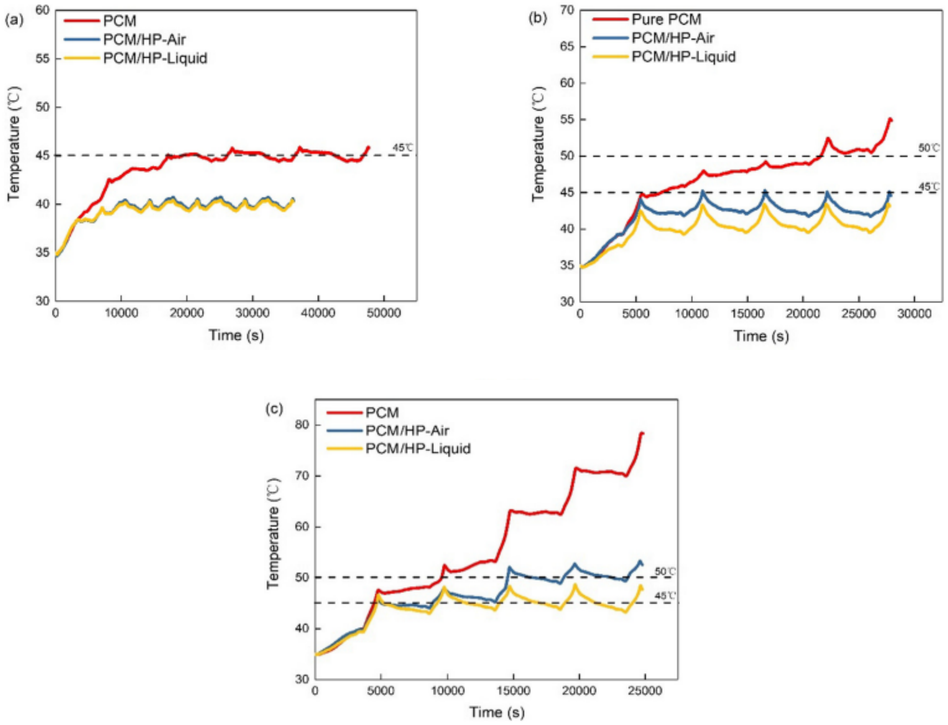

Figure 2.20: Temperature behaviour along time for different for different discharge rates: a) 1C ; b) 2C ; c) 3C [18]

2.7 Pulsating Heat Pipes

Pulsating Heat Pipes (PHP) are the last evolution of HP technology. They present a cheap, simple and flexible layout composed of tubes in a horizontal serpentine arrangement. The working fluid is used at saturation conditions with small vapour quality, alternating between its liquid slugs and vapour plugs as one can understand from Figure 2.21.

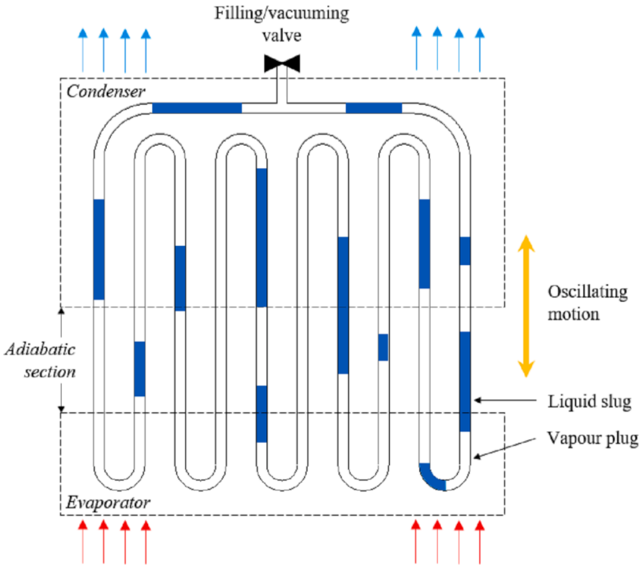

Figure 2.21: Working scheme of simple closed PHP application [33]

This kind of technology is also called of oscillating heat pipes because the circulation of the working fluid through the evaporator, where the fluid absorbs heat, triggers the expansion of the vapour plugs at the evaporator and consequently move the liquid slugs. This unbalances have the power to drive the system, where there is no need for auxiliary components, such as pumps, to make the fluid move through the closed loop. It is called as thermally driven device because these small instabilities make the system equalize the internal pressure, in order to balance them, what generates a self sustained motion as a result [33].

Before being filled with the working fluid, the pipes must be vacuumed first and then partially charged. This detail is important to avoid the presence of Non-Condensable Gases (NCG), which might impact in a negative way by increasing the saturation temperature and internal pressure of the biphasic fluid. The PHP thermal performance is affected by the inhibition of nucleation and bubble expansion as a consequence of the presence of air that can remain in the pipes if the process is not attended properly [36, 33].

Weixiu Shi et al (2023) studied the influence of cooling water flow rate at the condenser section using PHP. In this work it was analysed for different flow rates under different inclinations (influence of gravity). The scheme on Figure 2.22 represents the system principle with the instrumentation that collects the temperatures at strategic locations.

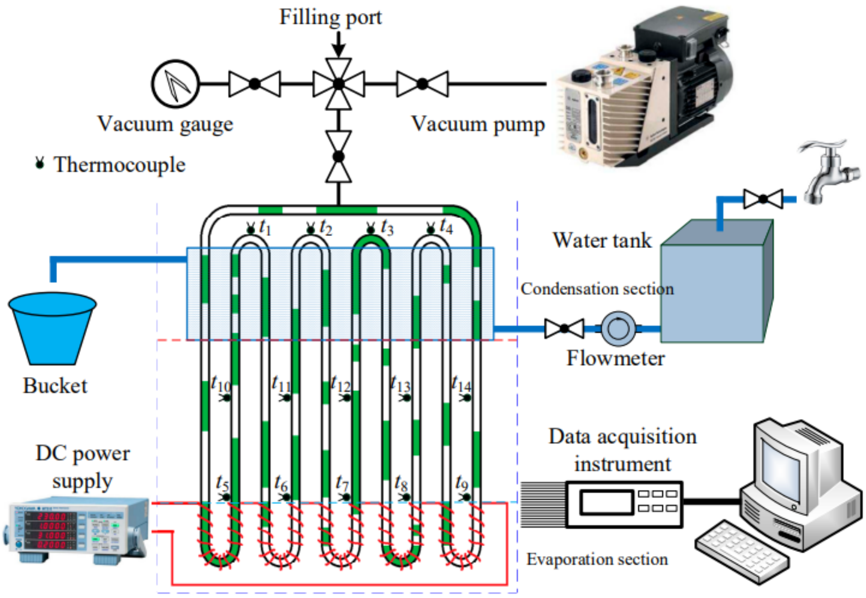

Figure 2.22: Experimental scheme using cooling water on PHP [35]

The low flow rate of 6.7 g/s leads to very slow values of heat dissipation at the condenser section. The mass flow rate of cooling water impacts in the pressure difference formed between the evaporator and the condenser, where if it increases it will aid the circulation of working fluid inside the closed loop PHP [35].

One of the other observations made was that under 90 W of heat power input, the best heat transfer performance was obtained for 9.7 g/s. However, for the higher values of heat power input it was for 6.7 g/s that the results shown the lowest thermal resistance value. Therefore, as one can think that increasing mass flow rate ensures better heat transfer performance, the authors state that there could exist a value that optimizes it and matches the heat dissipation requirements to be in consonance to a "better running effect" [35].

From the graphs in Figure 2.23 there are represented the wall temperatures evolution in time for a constant increase in heat power input, at 90º and 30º inclination. The tests were done with another proposal of evaluate the influence of gravity while decreasing the inclination from 90º to 60º and then to 30º, where the first position represents the horizontal orientation and the last one a position more close to a vertical orientation (more influence of gravity). By the results presented, it is noticeable the operation was poorer when the inclination is 30º and one obtains 110ºC of evaporator wall temperature for the lowest mass flow rate and the highest heat power input of 208.5 W.

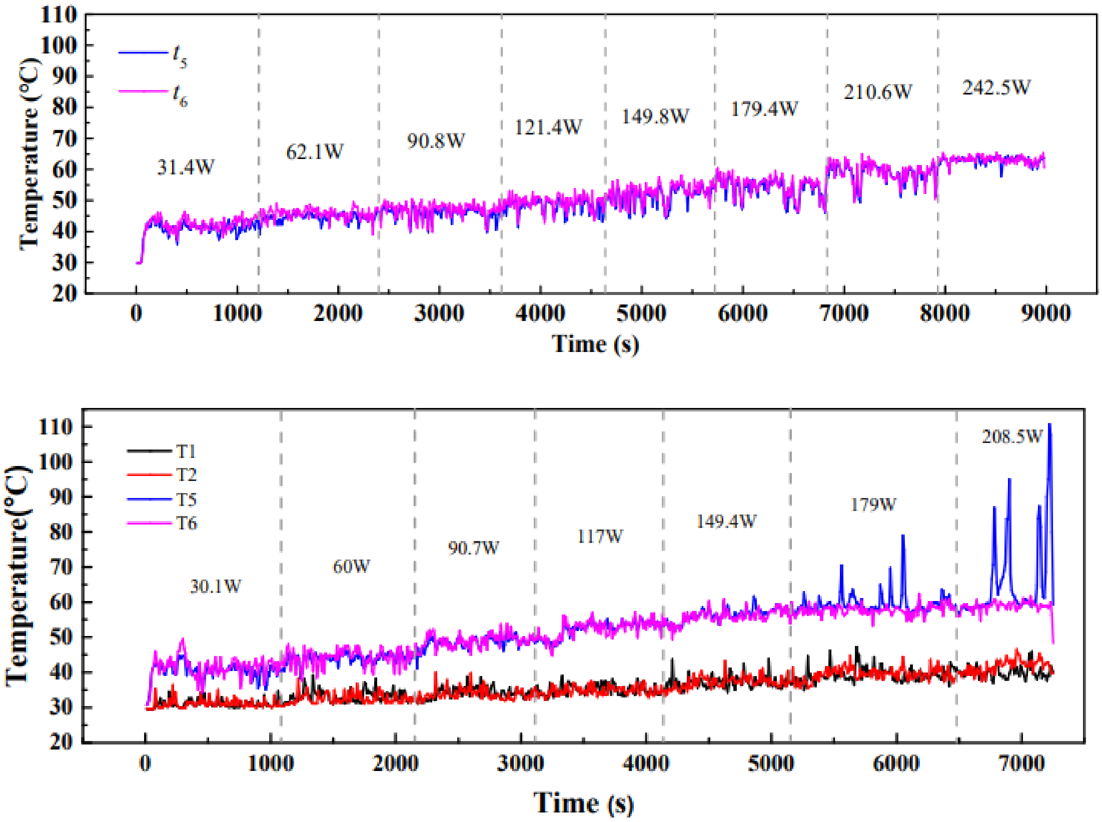

Figure 2.23: Evaporator wall temperatures for 90º (up) and 30º (down) angles at 6.7 g/s mass flow rate [35]

The disadvantages of adopting PHP are primarily associated with its implementation on systems with low heat demands. Although in this kind of applications high-frequency oscillations are present, the resulting fluid displacement are very small, leading to hindered flow. The application of PHP is still being studied as there are some challenges associated to the chaotic nature of the working fluid oscillations, causing dissimilarities in heat transfer capabilities in each channel, that are not yet understood. Additionally, as it uses a mixture of fluids in different physical states is difficult to describe accurately the mechanisms of heat transfer at its sections, either being free convection with air or forced convection with fluid.

Another significant issue lies in the definition of equivalent thermal resistance in PHP. The combined behaviours in its operation makes the thermal resistance equation too generalized, hampering the possibility for quantitative comparisons between different apparatus as the working fluids are not the same or even the pipes geometries and heating/cooling loads. This is also a drawback as there's still a lack of comprehensive description regarding its operational limits [33].

Chapter 3

Methodology

3.1 Power Dissipation of Lithium-ion Cell

The estimation of the thermal power dissipation of a lithium-ion cell can be done using the Equations 3.1, 3.3 and 3.4 as refereed in some articles [8, 25]. Sometimes, the technical specifications of the cells do not provide sufficient information about how the open circuit voltage (U_{OC}) varies with the temperature in which the cells are used. However, it is possible to find in some websites databases, such as in [23], where some experiments were done to obtain the behaviour of the cells voltage during its charging and discharging cycles.

$$\dot{Q}_{irr,i} = R_{int,i} \cdot I_i^2 \tag{3.1}$$

$$R_{int,i} = \frac{U_{ref} - U_i}{I_i - I_{ref}} \tag{3.2}$$

Regarding Equations 3.1 and 3.2, for each discharging current i, it is going to be used the respective discharging resistance ($R_{int,i}$), considering the reference discharging states. The calculation of the discharging resistance is defined by the quotient between the voltage difference and the correspondent current difference.

$$\dot{Q}_{rev,i} = I_i \cdot T \cdot \frac{\delta U_{oc}}{\delta T} \tag{3.3}$$

$$\dot{Q}_i = \dot{Q}_{irr,i} + \dot{Q}_{rev,i} \tag{3.4}$$

As a matter of example to proceed the power dissipation estimation, the Figure 3.1 of the Molicel INR- 21700-P42A cell presents a curve for a discharging cycle at a very low current. In fact, this current will lead to a complete discharge of the cell after a very long time, meaning it can be referred as a reference discharging current where the loss of electro-chemical power is almost zero. On the other hand, there are other discharging currents that expose the cell to more intense mechanisms of power loss as its value increases. In this way, the difference between the energy displayed by the other discharging currents and the energy displayed by the reference current can offer a way of calculating the heat losses in the cell, depending on using profile during the race.

The following Equations 3.5 and 3.6 transcribe the procedure explained before, where in the Annexes A.2 and A.3 is shared the MatLab code for data import from Excel and its data treatment to present the graph in Figure 4.2 at Section 4.

$$E_{loss,i} = \int P_{ref}\ dt_{ref} - \int P_i\ dt_i \tag{3.5}$$

$$E_{loss,i} = \int U_{ref} I_{ref}\ dt_{ref} - \int U_i I_i\ dt_i \tag{3.6}$$

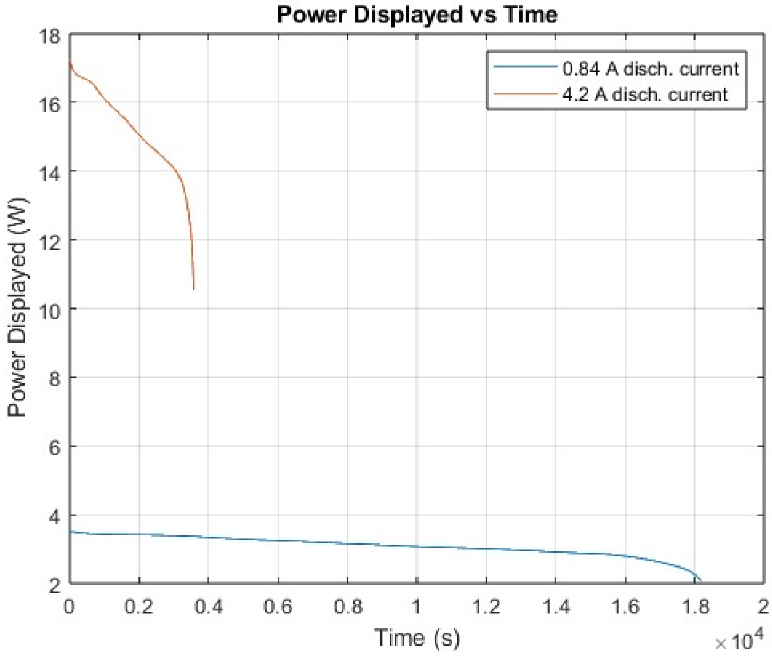

Figure 3.1: Power displayed over time for 0.84A and 4.2A discharge currents for Molicel INR-21700-P42A

The same approach was applied for the rest of the studied cells. The results were converted into energy loss per second, and at the end, for each one of them, it was possible to fit into a polynomial function the description of the behaviour of power loss with current intensity. The graph on Figure 3.2 gathers the curvatures for the different models of cells. Despite of the fact that the Molicel cells release less heat than the rest of the cells, the certification that they can supply the power demand of the electrical motors must be guaranteed.

3.2 Endurance Power Demand

The database in UNIPR Racing Team's drive complies all information for every Formula Student season. The information complies, technical data of used equipments, design projects and also extensive tracked data during the competition such as motor speed, braking pressure, battery power, and also current pattern.

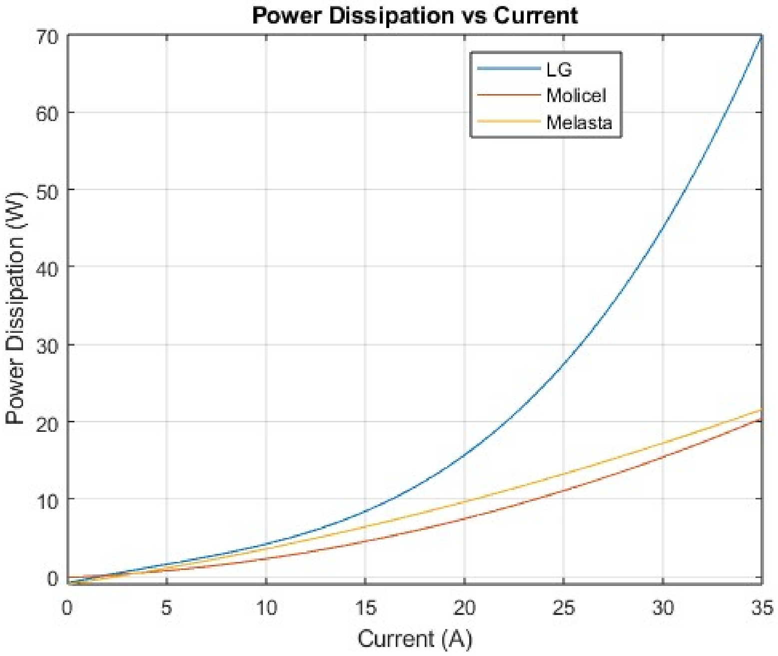

Figure 3.2: Power dissipated by the different lithium-ion cells

The process of calculating the endurance power demand is done firstly by filtering and smoothing the signals using the Savitzky-Golay Filtering (SGF) function from MatLab. The signals that come out from Vehicle Control Unit (VCU) are noisy, in this way, the SGF, also called as least-squares smoothing filters, preserves high frequency components getting rid of some of the noise [26]. After filtering, the MATLAB code in Annex A.4 selects data from the two halves of the endurance race, with the driver's exchange marking the transition to the second half. It then calculates a current average per second from the 10Hz tracked data.

In Equation 3.7 is described the way the current weighted average is calculated in order to use it as an estimation of the cooling needs of the battery pack.

$$I_i = \frac{\int I \, dt}{t_f - t_i} \tag{3.7}$$

One can depict from Figure 4.3 the current demand in each second for the two halves of the competition and then arrive at the power dissipation by applying the polynomial functions described before. The Figure 3.4 joins the power dissipation behaviour of the two moments of the competition for the LG cells, as they were the ones used in the previous season and made possible to track the presented data.

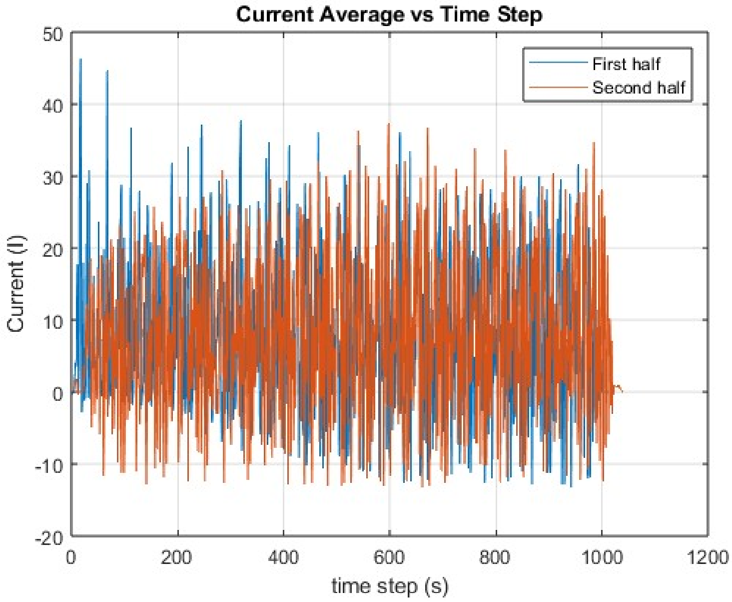

Figure 3.3: Current demand for each one of the half parts of the endurance competition on season 2022/2023

Also it is important to note that the negative values of current exist due to the regenerative breaking. When the driver lifts his foot from the gas pedal it is generated power being that the reason why the direction of the current is inverted.

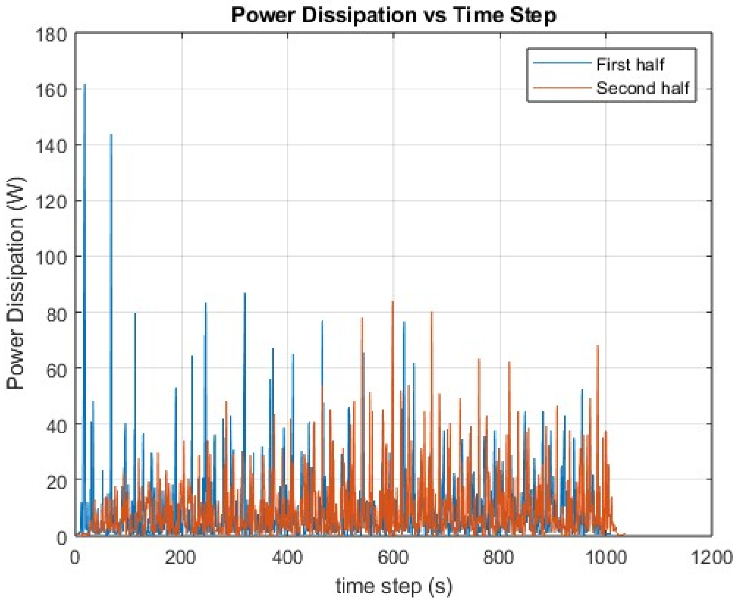

Figure 3.4: Power dissipation at each one of the half parts of the endurance competition using LG cells

3.3 Current Conversion for new Cells

As it was mentioned before, the estimation of the power dissipation is dependent on the use of current. The fact that the cells in study are displayed in different assemblies, i.e., with different number of cells in parallel and series, the data of current must be corrected. The correction is served by VCU data, regarding the state of charge and battery power display. The conversion is defined by the following equations and, more upfront, one will discuss and analyse its results.

$$P = I_{eff} \cdot U_{eff} \tag{3.8}$$

$$P = I \cdot (U_{bat} - RI) \tag{3.9}$$

$$RI^2 - U_{bat} I + P = 0 \tag{3.10}$$

Being P the battery power, I_{eff} the current that comes out to the load and U_{eff} the respective voltage. U_{bat} and R stands for the voltage and equivalent resistance of the battery, and I corresponding to the current in the circuit, being the same as I_{eff} as one can see from Figure 3.5.

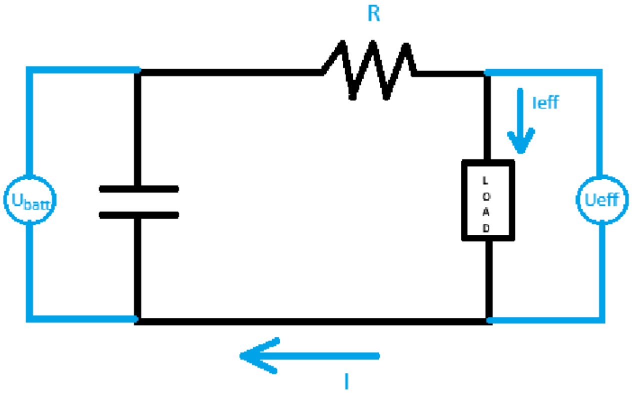

Figure 3.5: Draft of the formulation for current conversion

Applying the second order solving equation, it comes that:

$$I = \frac{U_{bat} \pm \sqrt{U_{bat}^2 - 4RP}}{2R} \tag{3.11}$$

Using cell parameters,

$$I = \frac{U_{cell} \cdot N_s \pm \sqrt{(U_{cell} \cdot N_s)^2 - 4R_{cell} P \cdot \frac{N_s}{N_p}}}{2R_{cell} \cdot \frac{N_s}{N_p}} \tag{3.12}$$

Where U_{cell} stands for voltage of the cell, N_s the number of cells in series, N_p the number of cells in parallel, R_{cell} the nominal cell impedance.

3.4 Implementation in EES

3.4.1 Cooling needs of the Battery Pack

After being observed the spectrum of the cooling needs during the race it was made the weighted-average of the power dissipation to the sizing of the cooling system. The system was modelled as a flow across tube banks as it is presented in Figure 3.6. As mentioned before, the alignment layout was preferred as it presents better heat transfer performance. Moreover, when air passes through the tube banks, the flow section is decreased which leads to an increment of the flow velocity. It is among the tube bank where the velocity of air reaches its higher velocities and those values are the ones that are used to calculate the Reynolds number (Re).

As the number of rows increase it is expected that the turbulence effects and heat transfer coefficient also increase. The author also states that after few rows, at the upstream side, there isn't such a significant change in turbulence level what makes the heat transfer coefficient remaining constant [48]. The problem itself is too complex to be solved via analytical methodology, so there were developed several correlations that make possible the calculation of the Nusselt number (Nu). In Equation 3.21 it is shown the correlation used in the calculations. Additionally, there are presented other equations written in the Engineering Equation Solver software (EES), e.g., the estimation of surface temperature of the tube banks, the average temperature used in air properties calculations, the log mean temperature and the heat transfer coefficient, which define the problem modulation and leads to the final solution.

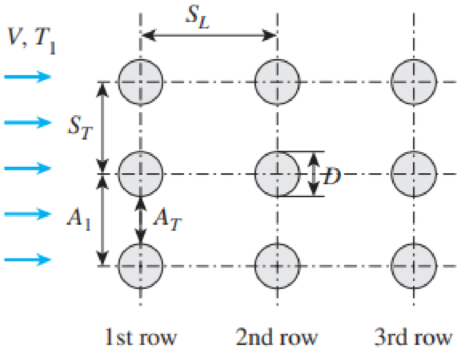

Figure 3.6: Flow across aligned tube banks [48]

Heat transfer equations on bank tubes

$$S_T = D + a_T \tag{3.13}$$

$$A_s = N\pi DL \tag{3.14}$$

$$\dot{m} = \rho V (N_T S_T L) \tag{3.15}$$

$$t_m = \frac{t_e + t_i}{2} \tag{3.16}$$

$$t_e = t_s - (t_s - t_i) \cdot exp\left(\frac{-As \cdot h}{\dot{m} \cdot cp}\right) \tag{3.17}$$

$$\Delta T_{lm} = \frac{(t_s - t_e) - (t_s - t_i)}{ln[(t_s - t_e)/(t_s - t_i)]} \tag{3.18}$$

$$V_{max} = V \cdot \frac{S_T}{S_T - D} \tag{3.19}$$

$$Re = \frac{\rho \cdot V_{max} \cdot D}{\mu} \tag{3.20}$$

$$N_u = 0.27 \cdot Re^{0.63} \cdot Pr^{0.36} \cdot \left(\frac{Pr}{Pr_{sup}}\right)^{0.25} \tag{3.21}$$

$$h = \frac{N_u \cdot k}{D} \tag{3.22}$$

$$\dot{Q}_{air} = h \cdot A_s \cdot \Delta T_{lm} \tag{3.23}$$

The implementation on EES, as shown in Annex B, is relatively simple after getting a better understanding on how does the modulation work. For the reduction of computational effort in these calculations and the ones made in the following section, one will take a look on how does the system behave in one of the battery's module. The Equation 3.18 has to be treated with a special care ensuring a temperature difference $(t_s - t_e)$ always higher than zero. Some problems might arise with the definition of the log-mean temperature difference for long number of rows in the longitudinal direction. As many rows are used in that direction, the more close the outlet temperature becomes to the surface temperature of the tube banks. With that, the equation is modified to the one in Equation 3.24 as it was done in [28]. That being said, the referred difference $(t_s - t_e)$ could be substituted by the correspondent value of 1% of t_s. Is worth commenting that the value is used as a practical rule and it can be arbitrary, as far it is in consonance with the physical sense of the problem.

$$\Delta T_{lm} = \frac{(t_s - t_e) - (t_s - t_i)}{ln[(t_s \cdot 0.01)/(t_s - t_i)]} \tag{3.24}$$

To make the resolution of the iterative solving effective it was created a parametric table in which it was evaluated the effect of air velocity in heat transfer. The values of air velocity chosen were 4.58 (low), 7.36 (medium) and 13.96 m/s (high), as the first value corresponds to the car stopped with its fans working, the second at a low vehicle speed and the last at its weighted-average speed. In Figure 3.7 it's depicted how is the vent system displayed in the battery case and in Figures 3.8 and 3.9 is shown the calculation of the air velocity for the small and the big fans.

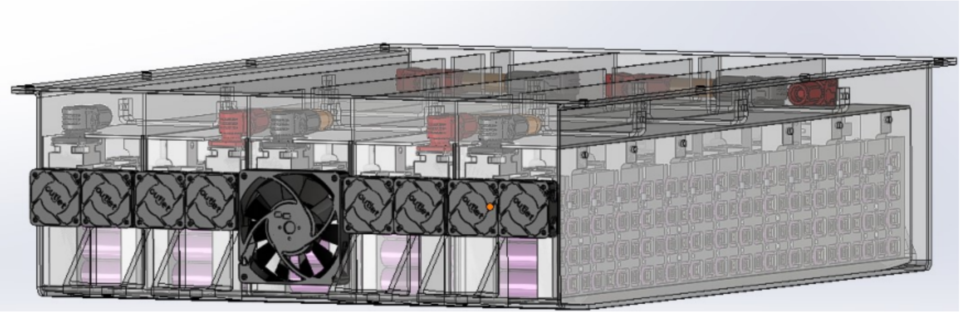

Figure 3.7: Ventilation in the battery case used in season 2022/2023 [31]

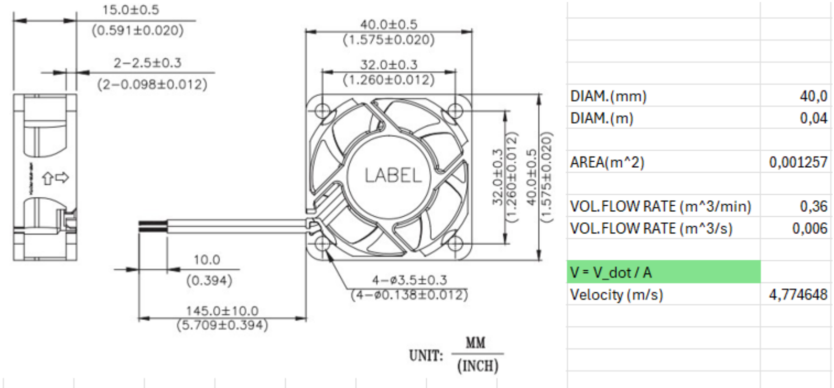

DIAM.(mm)	40,0
DIAM.(m)	0,04
AREA(m^2)	0,001257
VOL.FLOW RATE (m^3/min)	0,36
VOL.FLOW RATE (m^3/s)	0,006
V = V_dot / A	
Velocity (m/s)	4,774648

Figure 3.8: Speed calculation for Delta (40x40mm) EFB0412VHA [10]

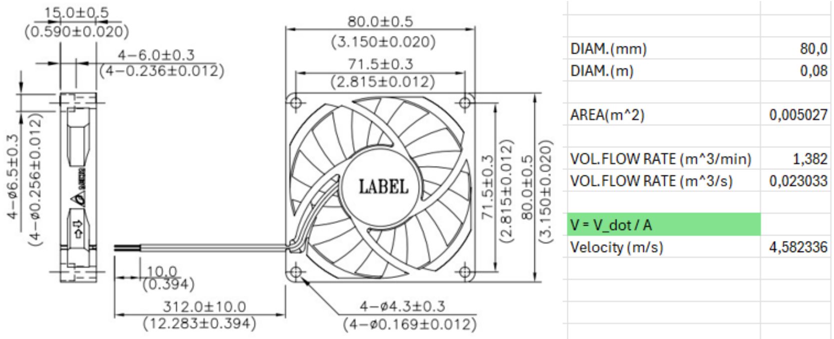

DIAM.(mm)	80,0
DIAM.(m)	0,08
AREA(m^2)	0,005027
VOL.FLOW RATE (m^3/min)	1,382
VOL.FLOW RATE (m^3/s)	0,023033
V = V_dot / A	
Velocity (m/s)	4,582336

Figure 3.9: Speed calculation for Delta (80x80mm) EFB0812HHB [11]

The air speed chosen for the conducted study was the one from the bigger fan because of its positioning in the middle of the battery pack and its lower value compared with the smaller fan. With the car moving and considering the environmental air static, the velocity it reaches the battery case can be set as the sum of the vehicle speed ($v_{vehicle}$) that one want to consider plus the speed of the fans working (v_{fan}). A low speed of 10 km/h (2.78 m/s) is chosen to study the cooling system behaviour to which the fan speed was added.

$$v = v_{vehicle} + v_{fan} \tag{3.25}$$

To calculate the weighted average speed of each half of the competition, the same methodology used in Section 3.2 was applied. Down in Figure 3.10 is shown the speed pattern during the race, arriving in the values of Table 3.1. The chosen value was of 9.38 m/s, corresponding to the second half. One more time here, the goal is to show in the following chapter that for the lower values of speed, in each proposed situations, one can be close with this approach to the temperature tracked data got from the previous season.

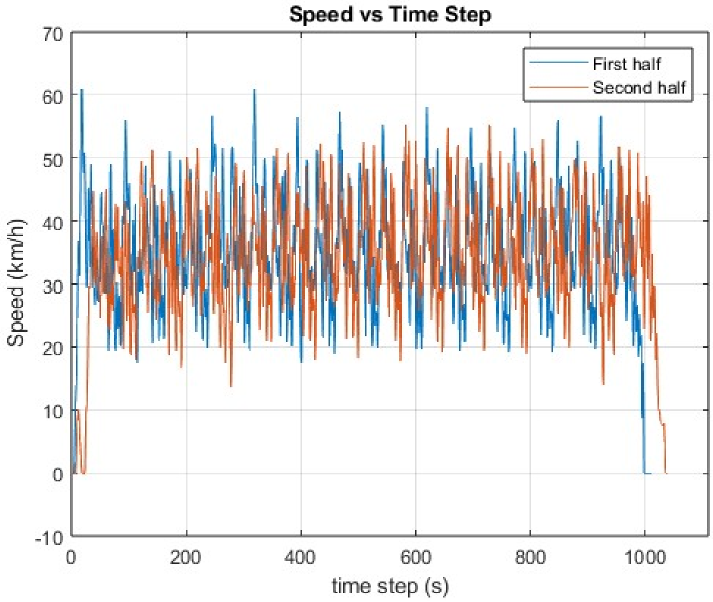

Figure 3.10: Speed patterns during the race in the 2022/2023 season

Table 3.1: Results of the weighted average speed during the race

Part of Race	Weighted-Average speed (m/s)
First Half	9.5909
Second Half	9.3760

3.4.2 Specific Heat of the cells

The type of chemistry used in the conceiving of a lithium ion cell dictates the way it is produced. As described in Chapter 2, in cylindrical cells the cathodes, anodes and separator are rolled up and then packed in case of that shape, in a similar way, the concept remains the same for the pouch cells. Moreover, if the specific heat needs to be calculated, or any other physical properties, one can consider a weighted average of the specific heats of each component and then arrive at the final value. However, by the type of chemistry and the capacity the cell displays one can search for some bibliography and use them as a source for those reference values to accomplish the goal of this work. In Table 3.2 are resumed all the values of cells properties.

Table 3.2: Some physical properties of lithium ion cells in study

Cells	LG 18650HE2	Molicel INR-21700-P42A	Melasta SLPBB042126
Sources	[46]	[46]	[13, 17]
Type of Chemistry	NMC	NMC	LCO
ρ (kg/m^3)	2708	2792	2261
c_p $(J/(kg\ K))$	953	1028	908
k $(W/(m\ K))$	14.2	15.2	2.95

3.4.3 Surface temperature of the cells

To make the model work, the temperature of the cells surface must be defined. Making use of Equation 3.26, the formulation is developed as follows:

$$\Delta Q = m \cdot c_p \cdot \Delta T \tag{3.26}$$

$$t \cdot \Delta \dot{Q} = m \cdot c_p \cdot (t_s - t_i) \tag{3.27}$$

$$t \cdot (\dot{Q}_{cell} - \dot{Q}^*_{air}) = m_{cell} \cdot c_p \cdot (t_s - t_i) \tag{3.28}$$

Where $\dot{Q}^*_{air}$ corresponds to the heat dissipated by air in each cell, being defined as:

$$\dot{Q}^*_{air} = \frac{\dot{Q}_{air}}{N} \tag{3.29}$$

So, joining Equations 3.28 and 3.29, it comes that:

$$t_s = t_i + \frac{t \cdot (\dot{Q}_{cell} - (\dot{Q}_{air}/N))}{m_{cell} \cdot c_p} \tag{3.30}$$

The creation of the parametric table allowed to see the evolution of the cells surface temperature (t_s) through time as the values were calculated in equal time steps from the beginning to the end of each one of the halves of the competition. More upfront to compare results, the second half is going to be selected as it presents higher cooling needs as one will conclude from Table 4.2. In the parametric table, there are also included some variables relevant to this study, e.g., ΔT_{lm}, h, t_e, t_s, $\dot{m}_{air}$ and $\dot{Q}_{air}$.

After the procedure, the results of the cell temperature were compared, aiming to get the value of air speed that could match the the cooling needs of the battery pack and prevent the temperature of the cell from rising in an unmanageable way.

Parametric Table

res

2..150	1 dtime [s]	2 $\dot{q}_{air}$ [W]	3 dtlm [K]	4 h [W/(m2 K)]	5 $\dot{m}$ [kg/s]	6 te [ºC]	7 tm	8 ts [ºC]
Run 141	979	992,7	3,77	639,6	0,08193	42,06121	35,53	42,62
Run 142	985,8	993,2	3,772	639,6	0,08193	42,06862	35,53	42,63
Run 143	992,6	993,6	3,774	639,6	0,08192	42,07594	35,54	42,63
Run 144	999,3	994,1	3,775	639,6	0,08192	42,08316	35,54	42,64
Run 145	1006	994,5	3,777	639,6	0,08192	42,09030	35,55	42,65
Run 146	1013	994,9	3,779	639,6	0,08192	42,09735	35,55	42,66
Run 147	1020	995,4	3,78	639,6	0,08192	42,10432	35,55	42,66
Run 148	1026	995,8	3,782	639,6	0,08192	42,11120	35,56	42,67
Run 149	1033	996,2	3,783	639,6	0,08192	42,11800	35,56	42,68
Run 150	1040	996,6	3,785	639,6	0,08192	42,12471	35,56	42,68

Figure 3.11: Parametric table showing temperature variation in time at high velocity

3.5 Ansys Fluent Implementation

3.5.1 Geometry

The modulation in Ansys Fluent was made in function of the geometry of each one of the three cells. In each study there was created an enclosure which has the goal to simulate the module geometry. One of its top was enlarged to evaluate what would be the temperature distribution in a section a few millimeters after the last row of cells. In the following Figures 3.12, 3.13 and 3.14 there are presented the apparatus of the modules and a description about its dimensions as well.

For the module of the LG cells, the enclosure was defined with (82 x 65 x 650)mm, being the first row of cells placed at 40 mm from the inlet and at 2 mm at both sides from the laterals. Then, the following rows were aligned and there were give a 2 mm spacing between cells.

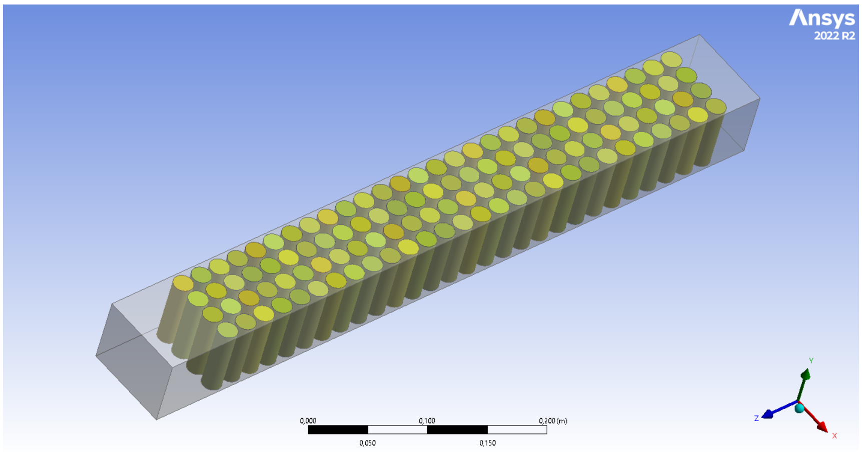

Figure 3.12: LG module geometry

The Molicel module was similar the one used for LG's, but this one had (71 x 70 x 380)mm as dimensions. The first row was placed at 40 mm from the intake being left 2 mm at both sides from the laterals as well. The rows that follow were spaced in 2 mm and aligned in z direction.

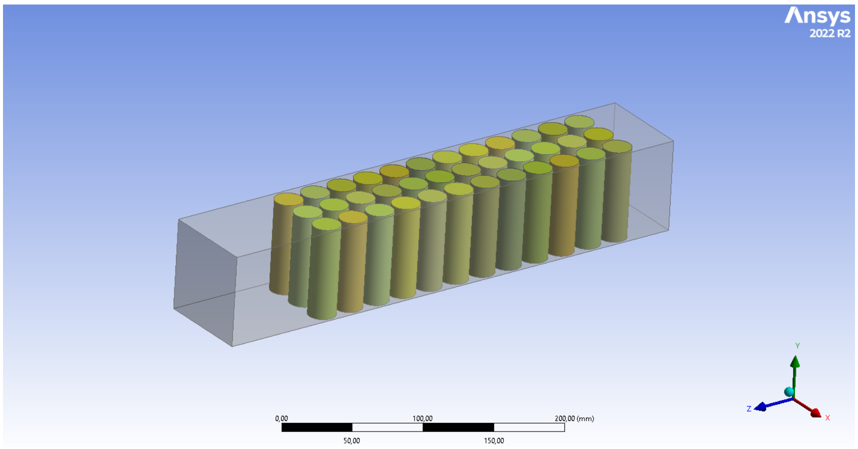

Figure 3.13: Molicel module geometry

The Melasta cells differ in its geometry as they are produced in pouch model. They were arranged in a "z" configuration as schematized in Figure 3.14, where, in all of its path the group of two cells are in series in groups of six.

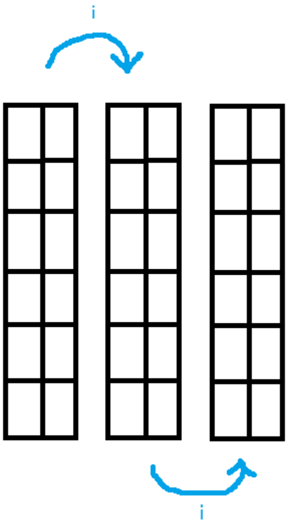

Figure 3.14: Scheme of the module's layout using Melasta cells

The enclosure was designed to replicate the module case with (69 x 150 x 370)mm, being the cells at 40 mm from the inlet and supported at 2.5 mm by the module's case (Figure 3.15). The cells in parallel are in direct contact with each other and with a 2 mm spacing to the following pairs.

All the geometries were specified accordingly its physical composition, being the cylinders treated as solids and the enclosure as fluid to make the CFD simulations work properly.

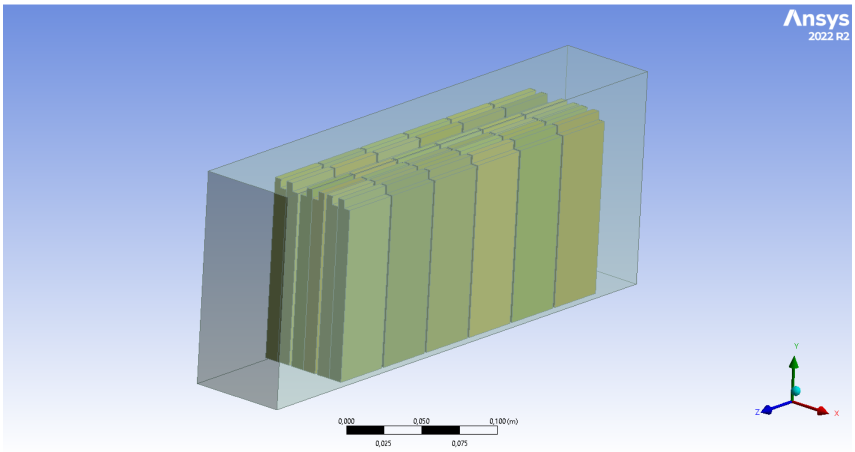

Figure 3.15: Melasta module geometry

3.5.2 Parametric Study of the Mesh

In order to make the simulations efficient in terms of computational effort, it was conducted a parametric study of the mesh. The main parameter studied was the number of elements and, in consequence, the maximum temperature one could achieve with it. There are presented in Table 3.3 the number of elements that are going to be evaluated. At a certain number of elements one will conclude the difference on the target number will not be meaningful anymore.

Table 3.3: Mesh Parametric study: number of elements evaluated

Mesh id	**1**	**2**	**3**	**4**	**5**
Number of Elements	907764	1256113	2003568	2445590	3151953

During the process of adding more elements to the mesh, some parametric values, such as orthogonal quality, aspect ratio, skewness and quality, will get finer. The better the parameters become while having a balance with the enough number of mesh elements, the better description of the phenomena one will get. With the desired number of elements it is going to be pursued a skewness average below 0.3 with a maximum number of 0.98 and an average orthogonal quality above 0.7 [12]. Additionally the Aspect Ratio one will looking for should not exceed 5:1 for cells away from the walls and 10:1 in the boundary layers [14]. In Figure 3.16 it is depicted mesh number 4 for the module with LG cells.

3.5.3 Setup definitions

At this stage of the modulation, it matters to use the proper models to describe the phenomena which one desire to study. To start with, there were allocated 16 processes in parallel with double precision for accuracy and stability of the numerical simulations. Enabling this option will enhance the convergence behaviour and reliability of its results at the cost of more processing time and memory usage.

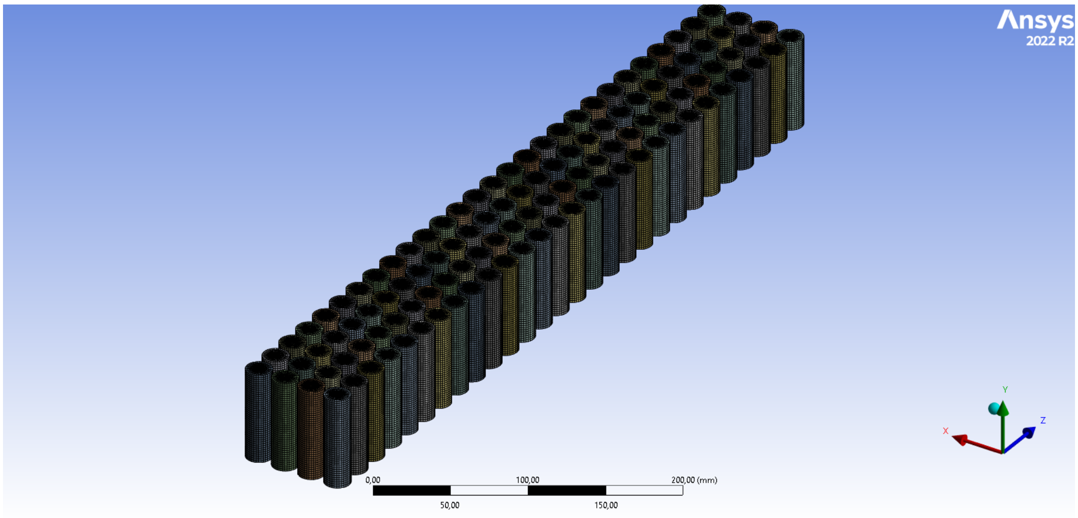

Figure 3.16: Generated mesh for the LG cells

The setup started with the use of the transient analysis to see the evolution in time of the cells temperatures. There were activated the energy equations and the viscous model chosen was the k-ω. This type of approach out-stands because of its higher accuracy in near wall regions, accounting more precisely for the viscous effects. The regions that surround the cylindrical cells can be considered as critic, i.e, the heat exchanges inside boundary layer regions are complex and, with that, as there are also high pressure gradients that need to be captured, this model can be present as a solution to it.

The shear stress transport was joined to combine both the $k-\omega$ and $k-\varepsilon$ models, making it more versatile and more suited for complex scenarios. Additionally, it was added a curvature correction factor of 1 that accounts for streamline rotations on curvatures on the turbulence structure.

In order to simulate the heat generated in the solid geometries, corresponding to the cylindrical cells, the source term input was selected to "1 source". Then it was specified as constant with the values displayed in Table 3.4, standing for the specific power generated (W/m^3).

Table 3.4: Specific Power dissipated for each type of cell

Cell	**Specific Power Dissipation (W/m^3)**
LG 18650HE2	574565.8
Molicel INR-21700-P42A	134472.0
Melasta SLPBB042126	87494.6

Finally, the inlet was defined with the mentioned velocities that one discussed previously and the outlet with 0 Pa of gauge pressure, being prevented the reverse flow through the module case. This option assures during the iterations that the flow does not reverse and start to come in from the outlet, which could affect the results in the regions that surround the outlet. Additionally, the surface boundaries of the module case are considered adiabatic, meaning they will not exchange heat with the outside environment.

3.6 NTC Thermistor

The battery case of the vehicle is equipped with NTC thermistors from Vishay. These components are made of a mixture of metal oxides, passing by a sintering process. They distinguish from other common temperature sensors, e.g., PTC, because of its behaviour directly related to the inverse of the temperature [41]. As the temperature increases, the resistance decreases, and that is even more noticeable for lower temperatures, where a small change leads to an higher variation of its resistance.

The characteristics of the NTC thermistor can be described as follows as a first approach:

$$R_t = R_o \cdot exp\left[B \cdot \left(\frac{1}{T} - \frac{1}{298.15}\right)\right] \tag{3.31}$$

Where R_o stands for the resistance at 25ºC and B the material constant expressed in Kelvin.

However, B varies with temperature and it can be calculated considering the resistances at 25 and 85ºC ($B_{25/85}$):

$$B_{25/85} = ln\left(\frac{R_{85}}{R_{25}}\right) / \left(\frac{1}{358.15} - \frac{1}{298.15}\right) \tag{3.32}$$

From [42] one can use the technical data from NTCALUG03A Mini LUG M3 shown in table 3.5.

Table 3.5: Electrical data of NTCALUG03A Mini LUG M3 [42]

R_o (Ω)	$B_{25/85}$ **(K)**
10000	3984

So the function's curve can be represented as it is depicted in Figure 3.17. From the technical sheet, in this range of temperatures, there is a thermal gradient of 0.02 ºC, i.e., the difference per each temperature degree between the temperature measured by the sensor and the real temperature of the surface.

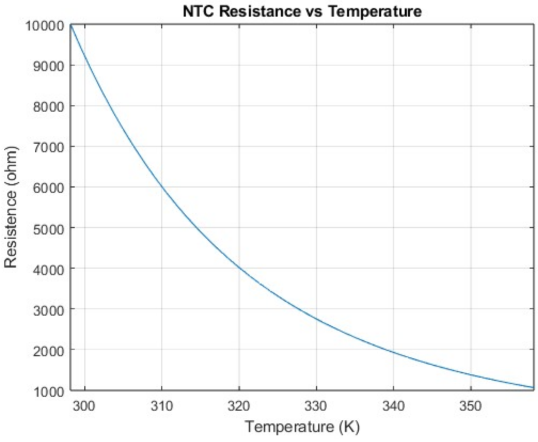

Figure 3.17: Resistance variation with temperature with NTCALUG03A Mini LUG M3

Chapter 4

Results and Discussion

4.1 Estimation on heat loss using Resistance analysis

As it was presented before, the estimation of heat loss in each cell was done by making the energy difference between the one at the current used at each time step and the one at the reference current. This methodology was applied as, not all the technical data for different lithium cells provide information regarding the variation of the U_{OC} with the temperature they were facing. However, for the Molicel cells, the producer provides that piece of information which is resumed in Table 4.1.

Table 4.1: Variation of U_{OC} with cells temperature [29]

Temperature (ºC)	Open-Circuit Voltage (V)
60	4.177
45	4.142
23	4.099
0	4.048
-20	3.988
-30	3.954

The present data was used in Matlab to give a clearer understanding on how does the U_{OC} increase with the increase of temperature, and, with that, applying a polynomial fitting of first order one could conclude about the good representativeness it provided. Figure 4.1 shows the curve equation and the r-square as well, and from the sensibility point of view is observed that at each one degree of temperature rise, the U_{OC} rises proportionally in 2.4 mV.

Summing up the curve obtained if only pure resistance was considered ($\dot{Q}_{irr}$) to the the term associated with the entropic term ($\dot{Q}_{rev}$) one can get a good approximation to the methodology that one wanted to validated, and was used for the rest of the cells. In Figure 4.2 there are depicted the three curves used to compare both mentioned estimations, where at 30A is obtained the maximum deviation from the values with a relative error of 8.45%.

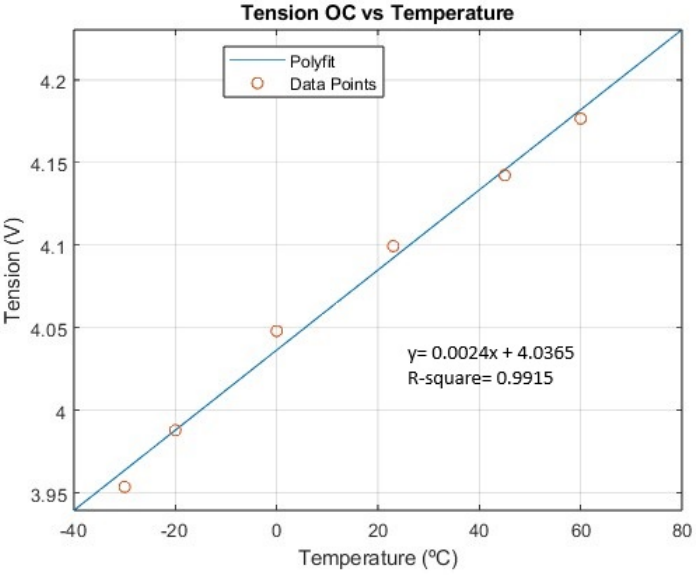

Figure 4.1: Best fitting curve for the data points in study

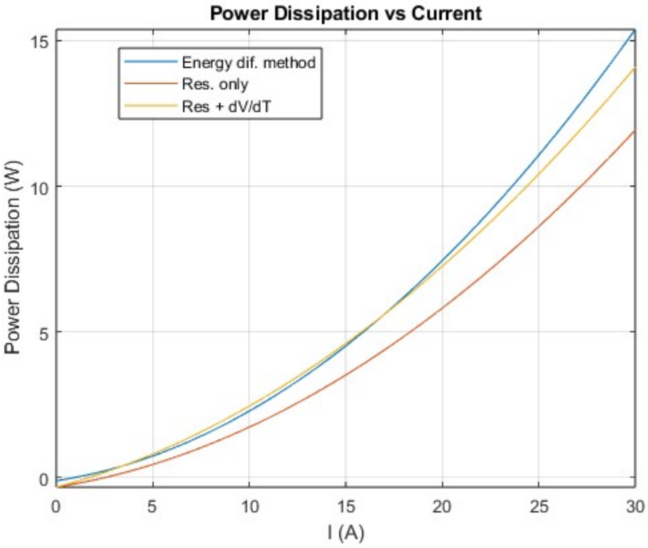

Figure 4.2: Power dissipated by the different lithium-ion cells using different methodologies

Despite the good approximation between the curves it is noticeable a small deviation when the current is higher than 20 A with a tendency to grow. However it is not a behaviour to be concerned about, making possible to conclude that the energy difference method can account for other loss mechanisms, such as the losing of electro-chemical potentials.

4.2 Endurance Cooling Needs

After applying the methodology of Sections 3.2 and 3.3 one was able to estimate the use pattern of current for the cells in study. Figure 4.3 presents the results obtained for the Molicel and Melasta cells. Table 4.2 summarizes the weighted-average in each half of the run for all the studied cells.

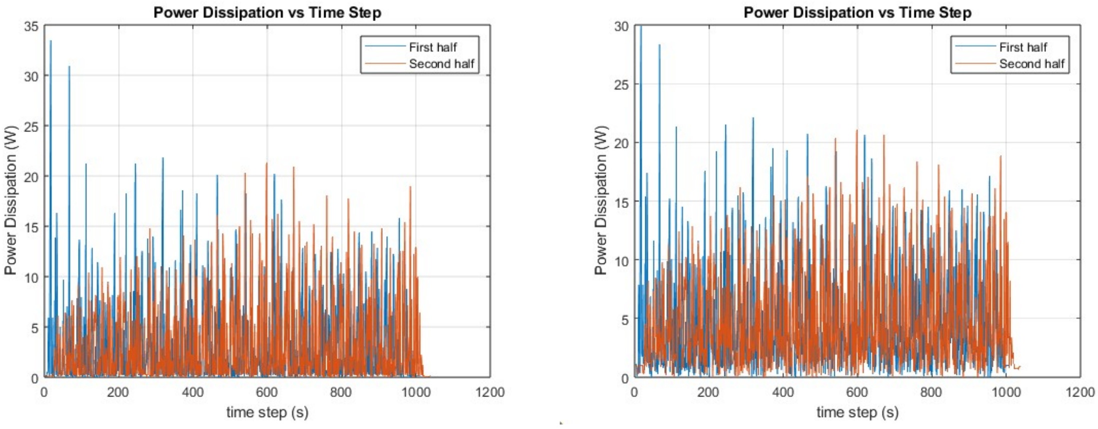

Figure 4.3: Power dissipated by Molicel cells (left) and Melasta cells (right) during two halves of the race

Table 4.2: Weighted-average power dissipation of all cells

Cell / Half	First	Second
LG 18650HE2	9.031 W	9.500 W
Molicel INR-21700-P42A	4.549 W	4.760 W
Melasta SLPBB042126	3.104 W	3.260 W

From the results obtained, the time average power dissipation that is going to be used in the simulations, makes the assumption that the cells will dissipate constantly the same amount of energy per second. To get a better idea if the cooling system is properly designed one will choose the higher amount of heat generated, being 9.500 W the power dissipated for LG, 4.760 W for Molicel and 3.260 W for Melasta.

One observation one can easily denote from Table 4.2 is the difference on the expected power dissipation from the LG to the Melasta cells, as there is a reduction of 65.6% and 49.8% from the LG to Molicel. This can be explained as the last two cells on the table display of higher capacities and with that, as one assume the same driving pattern, they won't waste the same amount of power as the LG cells would. The mechanisms of power loss are "enhanced", due to their higher capacities, which make their internal resistances lower than LG's and in consequence the power dissipated.

4.3 Parametric study of mesh

The results for the maximum temperature inside the module were obtained at the middle cells at its last row. It is shown in Table 4.3 how did the temperature changed as the number of elements increased.

Table 4.3: Maximum temperatures obtained in the module with the number of elements

Mesh id	**1**	**2**	**3**	**4**	**5**
Number of Elements	907764	1256113	2003568	2445590	3151953
Max. Temperature (ºC)	51.79	50.14	48.70	49.22	48.13

Plotting the values in Figure 4.4 one can see after mesh number 3 one could not need to use a finer one. The main reason for that is one would only augment the time of calculation and not obtain substantial changes for the computational effort that will occur during the calculation process. Although there is that computational limitation and the relative difference of the results from mesh number 4 to 5 is -2.21%, the value seems to converge to a value close to the temperature of mesh number 3. In fact the relative difference from mesh 5 to 3 is -1.17%, so, with that, one will opt to use it regarding its advantage on processing time.

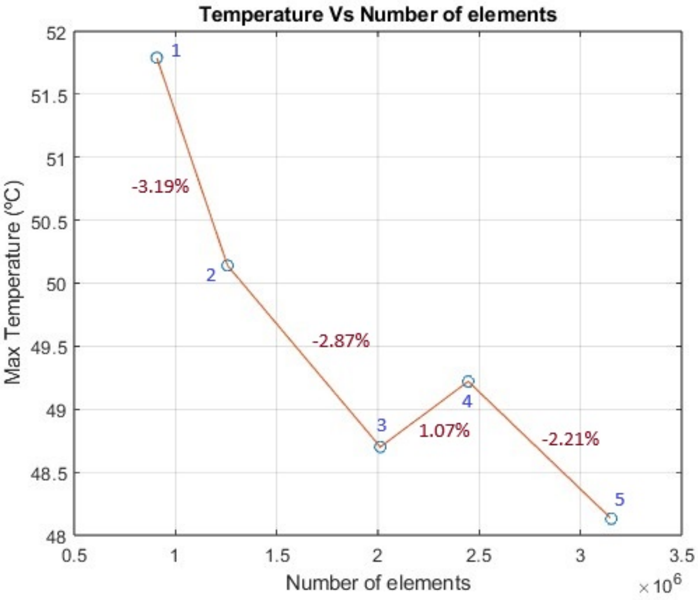

Figure 4.4: Relative differences of the maximum temperatures achieved

In what matters for the other parameters, the Table 4.4 presents the average values for each one of them. The maximum value for the skewness was 0.658 for only 210 elements (Figure 4.5 which is below 0.98, the maximum allowable value.

Table 4.4: Element metrics of studied mesh parameters

Parameter	**Element Metric (Average)**
Aspect Ratio	2.155
Skewness	0.128
Orthogonal Quality	0.979
Quality	0.745

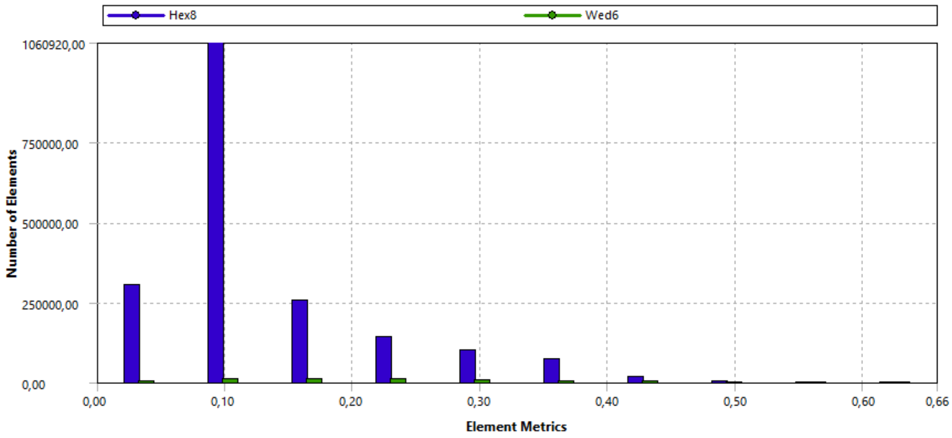

Figure 4.5: Skewness element metrics

Furthermore, the aspect ratio remained for a large number of cells below 5 as one observe from Figure 4.6, being even fewer the elements up to 9.04. In what regards the orthogonal quality, it is the most prominent value as it is well close to the ideal value of 1, with little elements that stay below 0.8 and above 0.52 (Figure 4.7).

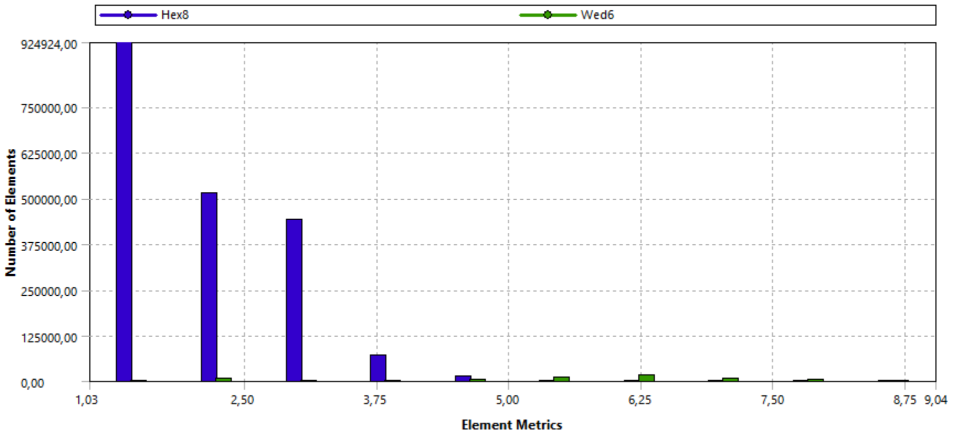

Figure 4.6: Aspect Ratio element metrics

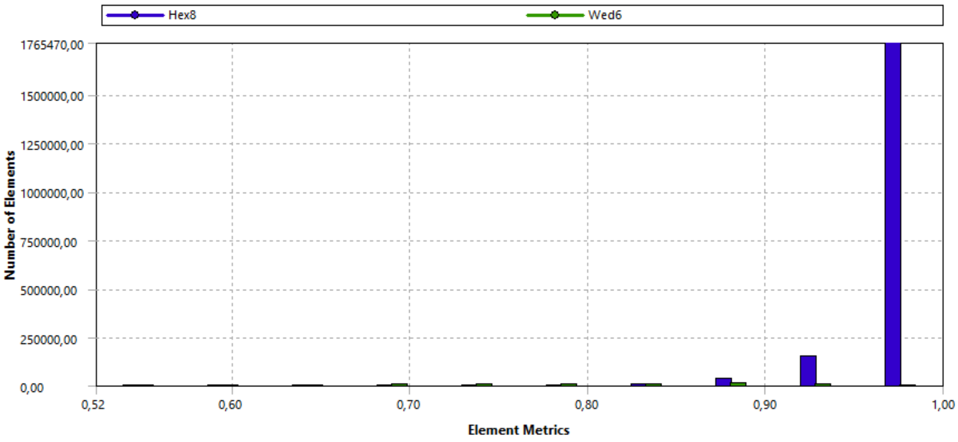

Figure 4.7: Orthogonal Quality element metrics

4.4 Results of temperature distribution and air flow inside the module on Ansys Fluent

At the end of the simulation, the distribution of temperature shows that the last rows of cells are the ones who display higher wall temperatures, more specifically the ones located at its central part. As one can see, the temperature gradient is depicted in Figure 4.8, where it is obtained a 10.34ºC of temperature difference in the battery module, at high speed. The first row of cells are the ones that have a different behaviour than the following rows, the reason that is behind the phenomena is related to the air speed, as big part of its contact area is cooled by air at a speed in which it enters in the battery case, i.e., the first row is cooled at a velocity lower than the rest of the cells. As the air circulates among the cells, the velocity increases because of the reduction of the passage area and, in consequence, is increased heat transfer coefficient which is related to it.

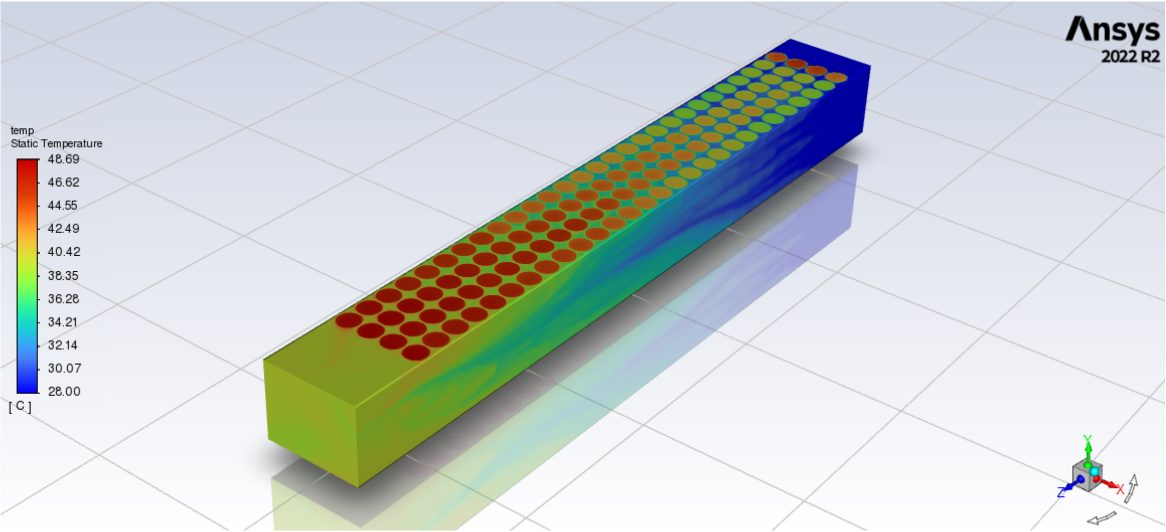

Figure 4.8: Temperature gradient inside the module at high speed

In what gives concern the air velocity, one see in Figure 4.9 what the formulation on Section 3.4 was referring to the speed which would be used for the calculation of the Reynolds number and, after that, to estimate the heat dissipated by air. The air at the inlet is kept constant and at the section of the last row of cells it's noticeable the air accelerates and reaches in the majority of the points around 90 m/s of speed.

4.5 Comparison of results of LG cells: Model validation

The results of the modulation in EES and in Ansys Fluent were plotted in Figure 4.10, where there was also included the values measured by the temperature sensors in the battery pack. From the graph is possible to notice a limitation of the models as they don't completely match the behaviour of the cells maximum temperatures. The main reason from which that occurs is related to the assumption that the cells would constantly dissipate the same amount of heat at a constant

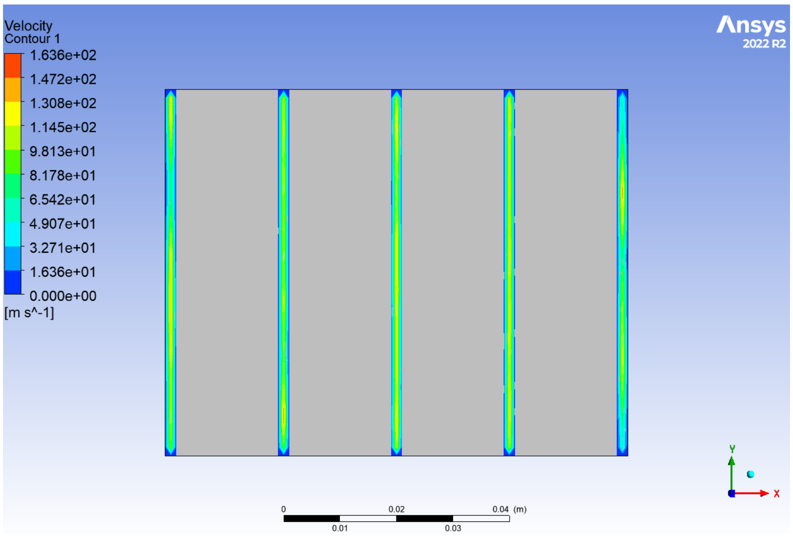

Figure 4.9: Velocity contour at the last row of cells

speed of air at the intake. For that reason, as it will be refereed more upfront, a tuned model, where one could describe in function of time the real speed of the car and the current that is going through each one of the cells, could be a good way to have a full description of the battery module behaviour.

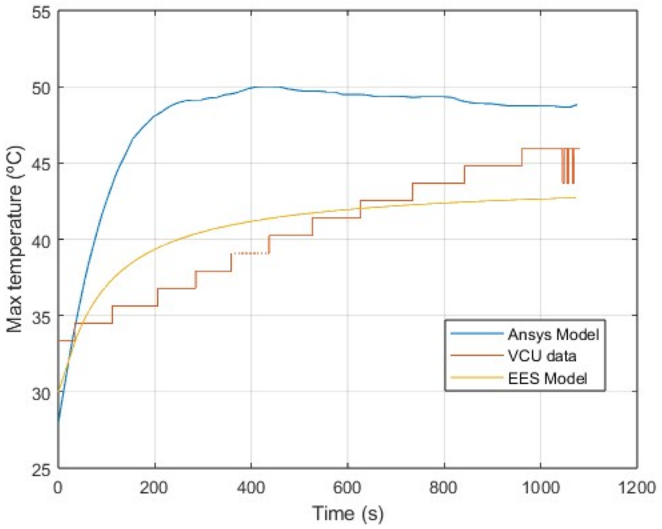

Figure 4.10: Comparisons between EES and Ansys models with real-time data

Although the drawback of the hypothesis chosen, the module applied on EES seems to represent more closely the behaviour of the cells temperature. At its end, the estimated temperature of the cells stays below the one it was registered. That could be explained by the assumption that on EES the heat dissipated by air is evenly distributed by all the cells, not existing any temperature difference between them. In Table 4.5 are resumed the three final temperatures and the respective relative errors.

Table 4.5: Results of final temperatures in each model

Models	**Temperature (ºC)**	**Relative Error (%)**
Temperature Sensors	45.93	-
EES	42.71	7.01
ANSYS	48.70	6.03

The values also show the amount of heat dissipated in each modulation was 1057.14 W and 996.6 W, for Ansys and EES respectively. In order to have a clue if the values are in a acceptable range of results, one looked at the literature for an example to use as a comparison mean. In [6], it is evaluated the cooling performance of Extended Range Electric Vehicles (EREV), which includes regular Electric Vehicles and its Plug-in hybrid versions. There were studied two concepts, one using fin design and the other channels design, where the air was in direct contact with the cells surface. These cells were 1.2 mm spaced and two heat generation rates were considered. One of them representing a regular driving pattern (500 W) and the other a peach load driving condition (1500 W). The results of the average air temperature are resumed in Table 4.6 for the pin-fin channel case concept.

Table 4.6: Results of average exit temperature at the two heat generation rates using different air flow rates [6]

Heat Generation (W)	**500**		**1500**	
Flow Rate (m^3/h)	100	200	200	600
Average exit temperature (K)	318.42	310.71	326.13	310.73

At 200 (m^3/h), the closest value of the work one elaborated (0.083 m^3/s), the average exit temperature is 310.71 K (37.56 ºC) and 326.13 K (52.98 ºC) for the regular and the peak load driving conditions, respectively. With this, as our heat production is between the values studied at the referred air flow rate, and the results are close the tracked data, one can validate the range of results obtained.

4.6 Molicel model results

In what regards the results obtained for the molicel cells, there is an approximation between the two methodologies used as the air velocity increases. That behaviour is denoted from Figure 4.11, where the final temperatures differ in 2.97ºC, 1.32ºC and 0.83ºC, respectively, from the situation with the lowest speed to the highest.

Additionally Figures 4.12, 4.13 and 4.14 show how is the temperature distribution along the module. Similarly to what happened with the LG cells, the first row of the cells are at slightly higher temperature due to a lower air speed and, the last cells at the module center the ones who also present higher temperatures.

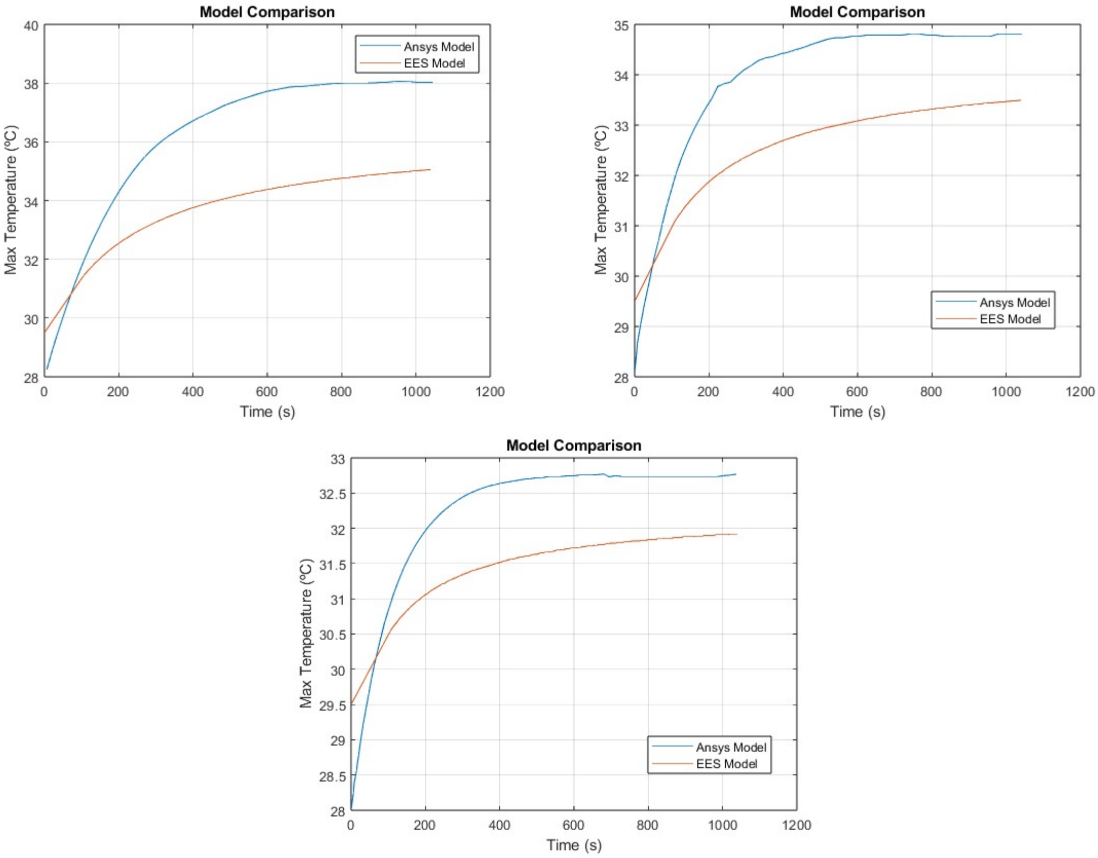

Figure 4.11: Temperature rise in Molicel cells in Ansys and EES at low (up left), medium (up right) and and high (down) air velocities

This suggests, by the temperature values, that the cooling system, as it is designed, ensures that the battery case works properly in the range of temperature that the literature suggests. The minimum and maximum cells temperatures for all different velocities are resumed in Table 4.7.

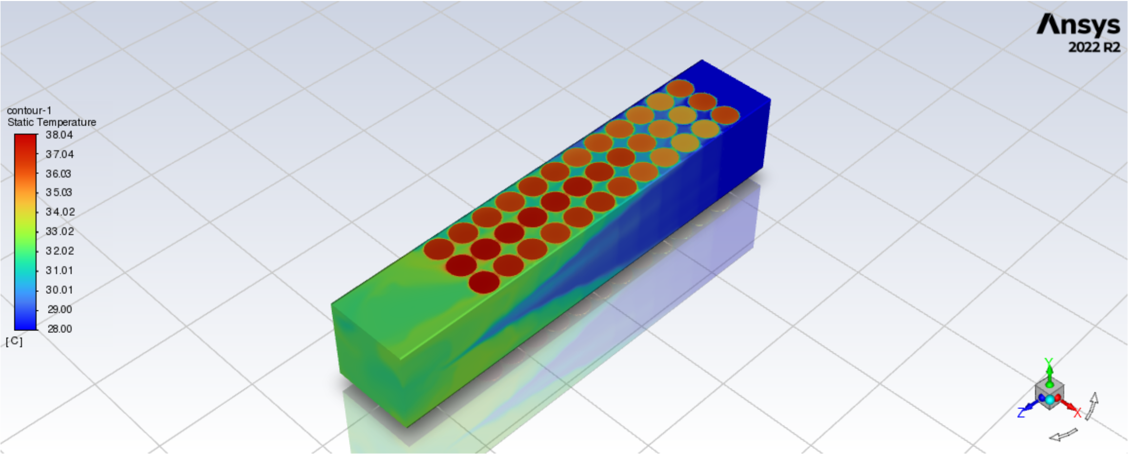

Figure 4.12: Temperature distribution for 4.58 m/s air velocity

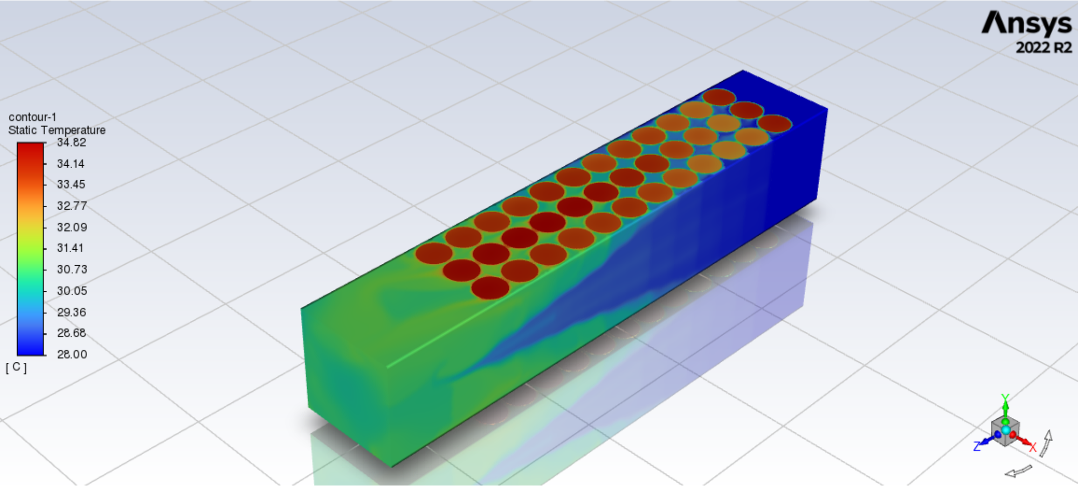

Figure 4.13: Temperature distribution for 7.36 m/s air velocity

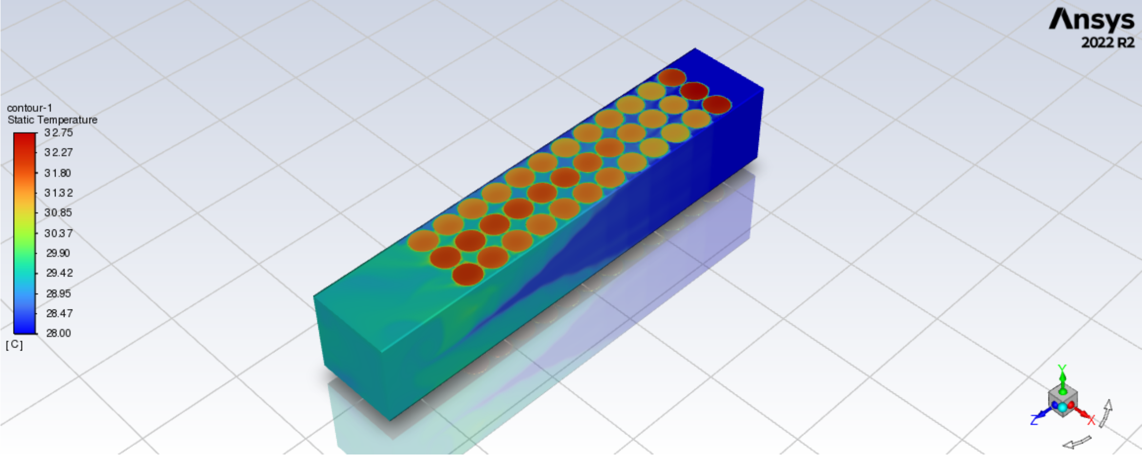

Figure 4.14: Temperature distribution for 13.96 m/s air velocity

The temperature difference has its maximum value at 4.58 m/s. Accordingly to the literature, the recommended maximum temperature difference throughout the cells that compound the module is 5ºC so, with that, all the values can be included in that acceptable range.

Table 4.7: Maximum temperature difference throughout the cells in the module at different air speeds

Air Speed (m/s)	**Temperature (ºC)**		**ΔT (ºC)**
	Min	**Max**	
4.58	34.18	38.02	3.96
7.36	32.32	34.81	2.50
13.96	30.70	32.75	2.05

4.7 Melasta model results

When studying the use of pouch cells it is noticeable a similar pattern of temperature rise. That pattern is, as one could expect, different from the one which described the behaviour of the cylindrical cells. In fact, they cannot be treated as tube banks anymore, as for the other examples, but as heat transfer with fins. Here, in this section one will only take a look to the results of the temperature rise at the studied speeds from the CFD simulations and conclude about their possible implementation. In Figure 4.15 there is depicted the temperature evolution and, even though, at the lowest speed the temperature value is under 48ºC, that ensures a margin of 12ºC to the maximum temperature allowable in formula student competitions.

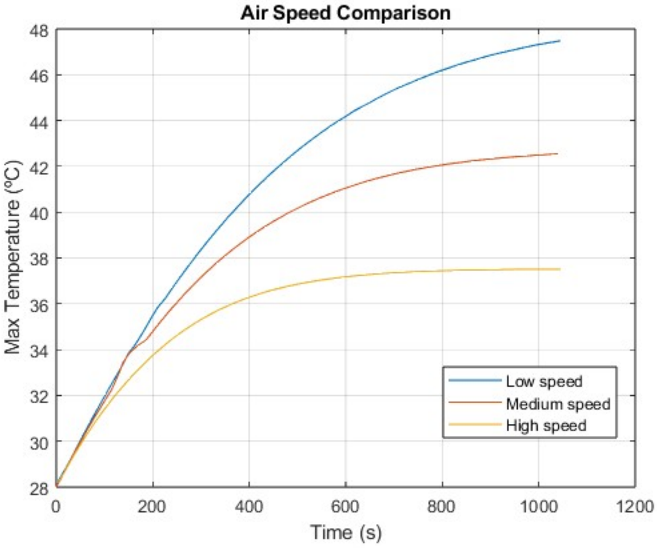

Figure 4.15: Maximum temperature using Melasta cells at different speeds at the air inlet

Furthermore, the results show for the medium and high speed that one can even place the temperatures inside the range that able its working with the best performance and with higher lifetime service (20-40ºC). In Figures 4.16 and 4.17 it is possible to see the temperature distribution in the pouch cells, as it happened for the cylindrical cells, the critical areas are located at the cells placed in the center of the module. There is an higher temperature difference from its core to its tabs, being the maximum temperature differences reported of 7.64ºC, 8.78ºC and 9.79ºC, respectively, from the highest to the lowest speed. These values are slightly above the temperature difference value that prevents the cells from malfunctioning, which also demonstrates the big importance of the cooling system. Although the temperature difference is still not to be concerned about in the case where the high speed is used, it is needed a good cooling capacity from its fans if one wish to keep the same air cooling system apparatus.

Comparing the results of this section and the previous one, one can have now an idea on how would these type of cells behave during the competition. If the power and capacity availability have an higher weight on the choice from one of the two possible cells at the expense of higher cell temperatures, the Melasta cells can be a solution, although some optimizations to the cooling

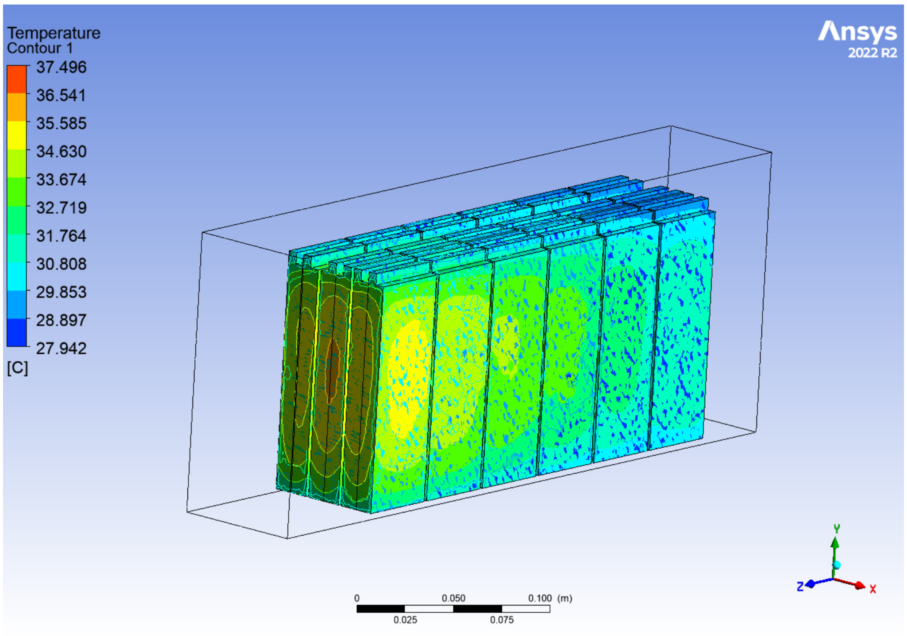

Figure 4.16: Temperature distribution on pouch cells at high speed

systems should be done. If the choice does not give to much importance to power and capacity displayed, in which it is preferred a more stabilized thermal behaviour and not proceeding too much changes to the actual cooling system, the Molicel cells can be presented as the best choice.

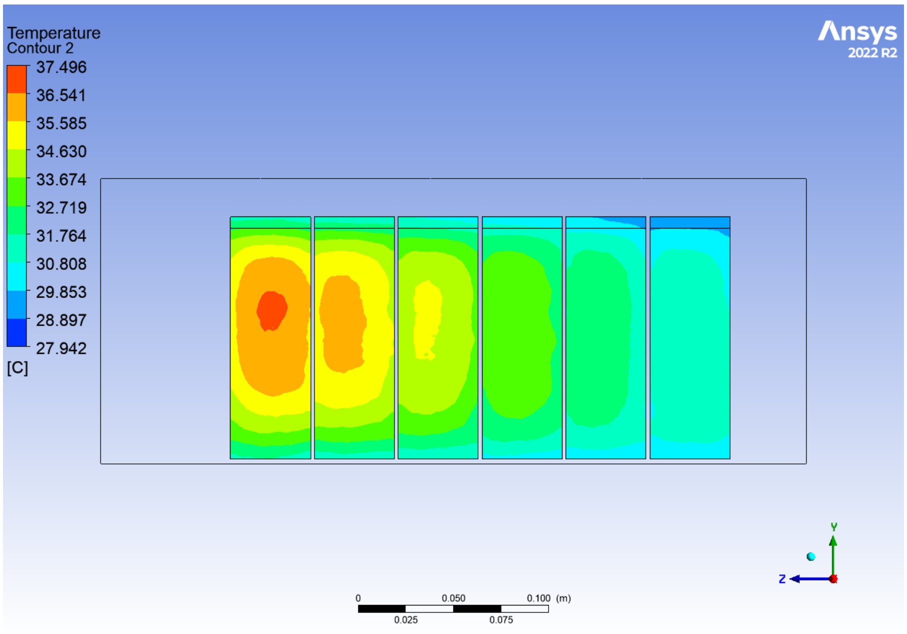

Figure 4.17: Temperature distribution on the pouch cells located at the center of the module (high speed)

Chapter 5

Conclusions and Future Work

5.1 Conclusions

In this work one is focused in comprehend how do the different types of lithium ion cells behave accordingly to the power demand during an endurance race. The scope of this investigation was developed in the formula student team of Università di Parma, with almost twenty years of history in this kind of competition.

One could understand from the literature the different technical characteristics of lithium-ion cells, the way they can be coupled to each other in order to meet the requirements of power and capacity and, at least if they are accordingly to the regulations that run the competition. The optimal range of cells temperatures (20-40ºC) was always considered during the development of the this work, where there were also analyzed some findings in air-cooling and liquid-cooling systems that were suited, more upfront, to the goals of the UNIPR Racing Team.

The methods used in this work to determine the heat generation present an alternative way to the use of electro-chemical models, being of a more simpler application. The results were close to the ones obtained by other authors when the working conditions specified by the producers are respected. Moreover, there were compared for the most demanding half of the race, in terms of cooling needs, the models in EES and Ansys Fluent. The findings shown a good approximation for the final temperature, and a reasonable time representation of the temperature behaviour. The module geometry used has the drawback of being long, which according to the CFD results of temperature distribution might arise some problems related to temperature differences inside the module case, and, consequently, in the electrical supply.

In what gives concern to the potential new cells, the Melasta cells can be an option for the big amount of power it can ensure, for rapid accelerations as matter of example. Although that feature can be taken as leverage, that is got at the expense of a slightly decrease in electric transmission efficiently. On the other hand, for a more stabilized functioning, while having an increased capacity compared to the last Formula SAE season, the Molicel cells can be the best choice as also, there will not be needed too much changes on the actual concept of the cooling system.

5.2 Future Work

In future works, it would be interesting to make experiments with the Molicel and Melasta samples, to evaluate how good the estimations are at predicting the amount of heat produced while working at different constant discharging currents. In that way, if one can access the voltage variation with cell capacity, one can easy and rapidly estimate the power dissipated by heat.

Regarding the EES modeling, a fin heat transfer analysis could be computed, matching the system requirements for the pouch cells in order to compare the results of Fluent. Also, regarding the cooling system of the pouch cells, one could think about implementing a system similar to the one presented in [6], using pin-fin geometries which increase the contact area, enhancing heat transfer, and improving the homogeneity of temperature in each cell.

In order to improve the description of temperature evolution when compared to the data recorded by the sensors and approximate the model to reality, future developments should include the integration of the real current pattern and the air speed at the battery case intake (tuned model) in Ansys Fluent.

Finally, regarding the additional weight of the system, one could investigate the integration of a liquid cooling system, using water, as the regulation states it as a legal working fluid. The system could make use of channels arranged in a serpentine, giving support to the existing air cooling system where it would be expected to have better overall performance. Another option could be the incorporation of a reciprocating cooling system, which could enhance the temperature homogeneity in the battery case.

References

[1] International Energy Agency. Iea, electric vehicles. https://www.iea.org/energy-system/transport/electric-vehicles, 2023. Acessed in January 2024.

[2] U.S. Environmental Protection Agency. Epa us06 or supplemental federal test procedures (sftp). https://www.epa.gov/emission-standards-reference-guide/epa-us06-or-supplemental-federal-test-procedures-sftp, May 2023. Acessed in February 2024.

[3] Hafiz Muhammad Ali. Thermal management systems for batteries in electric vehicles: A recent review. *Energy Reports*, 9:5545–5564, 2023.

[4] LiPol Battery. 15c high rate lithium ion battery| at lipol battery co.,ltd. https://www.lipobattery.us/high-rate-lithium-ion-battery-15c-2/. Acessed in April 2024.

[5] LG Chem. Product specification: Rechargeable lithium ion battery. https://www.powerstream.com/p/LG-ICR18650HE2-REV0.pdf. Acessed in April 2024.

[6] Kuo-Huey Chen, Taeyoung Han, Bahram Khalighi, and Philip Klaus. Air cooling concepts for li-ion battery pack in cell level. page V001T09A001, 07 2017.

[7] Projeto Experimentos de Física com Materiais do Dia-a Dia UNESP/Bauru. Associação de pilhas. https://www2.fc.unesp.br/experimentosdefisica/ele08.htm. Acessed in May 2024.

[8] Armando De Vita, Arpit Maheshwari, Matteo Destro, Massimo Santarelli, and Massimiliana Carello. Transient thermal analysis of a lithium-ion battery pack comparing different cooling solutions for automotive applications. *Applied Energy*, 206:101–112, 2017.

[9] Battery Design. Series and parallel. https://www.batterydesign.net/electrical/series-and-parallel/. Acessed in May 2024.

[10] Delta Electronics. Dc fans efb0412vha. online. Acessed in May 2024.

[11] Delta Electronics. Dc fans efb0812hhb. online. Acessed in May 2024.

[12] Bruno Veiga et al. *Study of the flow around a submerged submarine*. Faculdade de Engenharia da Universidade do Porto (FEUP), 2023. Private Document.

[13] Matthias Faber, Oliver Buitkamp, Simon Ritz, Martin Börner, Jonathan Berger, Julian Friedrich, Arno Arzberger, and Dirk Uwe Sauer. A method to determine the specific heat capacity of lithium-ion battery cells using thermal insulation. *Journal of Power Sources*, 583:233499, 2023.

[14] Ansys Fluent. Mesh quality. online. Acessed in May 2024.

[15] Tao Hai, Awatef Abidi, Azher M. Abed, Jincheng Zhou, Emad Hasani Malekshah, and Hikmet Ş. Aybar. Three-dimensional numerical study of the effect of an air-cooled system on thermal management of a cylindrical lithium-ion battery pack with two different arrangements of battery cells. *Journal of Power Sources*, 550:232117, 2022.

[16] Fan He, Haoting Wang, and Lin Ma. Experimental demonstration of active thermal control of a battery module consisting of multiple li-ion cells. *International Journal of Heat and Mass Transfer*, 91:630–639, 2015.

[17] Hanchi Hong, Xu Shi, Luigi d'Apolito, and Qianfan Xin. Immersion cooling for lithium–ion batteries at high discharging rates. 03 2024.

[18] Qiqiu Huang, Xinxi Li, Guoqing Zhang, Jiangyun Zhang, Fengqi He, and Yang Li. Experimental investigation of the thermal performance of heat pipe assisted phase change material for battery thermal management system. *Applied Thermal Engineering*, 141:1092–1100, 2018.

[19] SAE International. Rules 2024. online. Acessed in May 2024.

[20] Jiuchun Jiang and Caiping Zhang. *Fundamentals and Applications of Lithium-ion Batteries in Electric Drive Vehicles*. John Wiley Sons, 2015.

[21] Feng Leng, Cher Ming Tan, and Michael Pecht. Effect of temperature on the aging rate of li ion battery operating above room temperature. *Scientific Reports*, 5, 2015.

[22] Gabriele Leoncini, Ronan Mothier, Benoît Michel, and Marc Clausse. A review on challenges concerning thermal management system design for medium duty electric vehicles. *Applied Thermal Engineering*, 236:121464, 2024.

[23] lygte info. Index of tested liion batteries. https://lygte-info.dk/info/batteryIndex.html. Acessed in March 2024.

[24] lygte info. Lg 18650 he2 2500mah (red). https://lygte-info.dk/review/batteries2012/LG Acessed in March 2024.

[25] Rajib Mahamud and Chanwoo Park. Reciprocating air flow for li-ion battery thermal management to improve temperature uniformity. *Journal of Power Sources*, 196(13):5685–5696, 2011.

[26] MathWorks. Savitzky-golay filtering. https://www.mathworks.com/help/signal/ref/sgolayfilt .htmlReferences. Acessed in April 2024.

[27] Melasta. Product specification polymer li-ion cell 3.7v 6600mah 15c. http://www.melasta.com/. Acessed in March 2024.

[28] Moses Minta. Analytical and experimental studies of an optimum helium liquefaction cycle. *Massachusetts Institute of Technology*, July 1984.

[29] Molicel. product data sheet model inr-21700-p42a. https://www.molicel.com/wp-content/uploads/INR21700P42A-V4-80092.pdf. Acessed in March 2024.

[30] Dave Nichols. Greencars, different types of ev batteries. https://www.greencars.com/greencars-101/different-types-of-ev-batteries, June 2023. Acessed in February 2024.

[31] Chiappini Nicola. *IMPIANTI DI RAFFREDDAMENTO NELLE MONOPOSTO ELETTRICHE DELL'UNIPR RACING TEAM*. Università di Parma, 2023.

[32] OneCharge. Types of lithium batteries: Lithium cell format. https://www.onecharge.biz/lithium-cell-format/, 2024. Acessed in February 2024.

[33] Luca Pagliarini, Naoko Iwata, and Fabio Bozzoli. Pulsating heat pipes: Critical review on different experimental techniques. *Experimental Thermal and Fluid Science*, 148:110980, 2023.

[34] Samuele Piccinini. *Formula Student: dall'aula alla pista di gara*. Università di Parma, 2022.

[35] Weixiu Shi, Xuebing Liu, Xiaoyang Su, Hongdi Chen, and Lisheng Pan. Influence of cooling water flow rate on start and heat transfer performance of pulsating heat pipe at different inclination angles. *Sustainability*, 15(3), 2023.

[36] ACT Advanced Cooling Technologies. Pulsating heat pipes. https://www.1-act.com/thermal-solutions/passive/heat-pipes/pulsating/, 2024. Acessed in April 2024.

[37] HPT Heat Pipes Technology. Heat pipe principle and applications. https://www.heatpipe.com/engineering-manual/heat-pipe-principle-and-applications/, 2021. Acessed in April 2024.

[38] McGordon Andrew Low John C. T. Tripathy, Yashraj and James Marco. Low temperature performance of lithium-ion batteries for different drive cycles. *Electric Vehicle Symposium (EVS 29)*, pages 1–12, 2016.

[39] UNIPR. Unipr racing team - formula sae. https://www.uniprrt.it/it/home-it/, 2023. Acessed in February 2024.

[40] William James Valerie Volcovici, Gloria Dickie. Reuters, nations strike deal at cop28 to transition away from fossil fuels. https://www.reuters.com/business/environment/countries-push-cop28-deal-fossil-fuels-talks-spill-into-overtime-2023-12-12/, 2023. Acessed in January 2024.

[41] Vishay. Ntc thermistors. https://www.vishay.com/docs/29053/ntcappnote.pdf. Acessed in June 2024.

[42] Vishay. Ntc thermistors, mini lug sensors. https://www.vishay.com/docs/29114/ntcalug3.pdf. Acessed in June 2024.

[43] Jinhong Xie, Zijing Ge, Mengyan Zang, and Shuangfeng Wang. Structural optimization of lithium-ion battery pack with forced air cooling system. *Applied Thermal Engineering*, 126:583–593, 2017.

[44] X.M. Xu and R. He. Research on the heat dissipation performance of battery pack based on forced air cooling. *Journal of Power Sources*, 240:33–41, 2013.

[45] Wen Yang, Fei Zhou, Haobing Zhou, Qianzhi Wang, and Jizhou Kong. Thermal performance of cylindrical lithium-ion battery thermal management system integrated with mini-channel liquid cooling and air cooling. *Applied Thermal Engineering*, 175:115331, 2020.

[46] Hong Yu, Hengyun Zhang, Jinghe Shi, Shunbo Liu, Zhaozang Yi, Shen Xu, and Xinwei Wang. Thermal parameters of cylindrical power batteries: Quasi-steady state heat guarding measurement and thermal management strategies. *Applied Thermal Engineering*, 231:120959, 2023.

[47] Luyao Zhao, Wei Li, Guoyang Wang, Wenmin Cheng, and Mingyi Chen. A novel thermal management system for lithium-ion battery modules combining direct liquid-cooling with forced air-cooling. *Applied Thermal Engineering*, 232:120992, 2023.

[48] Yunus A. Çengel and Afshin J. Ghajar. *Heat and Mass Transfer: Fundamentals and Applications*. McGraw-Hill Education, 5th edition, 2015.

Appendix A

MatLab Code

A.1 Import Data Function

```matlab
    function ImportLG = importfile(workbookFile, data_col)

%% Input handling

% If no sheet is specified, read first sheet
sheetName = 1;

% If row start and end points are not specified, define defaults
dataLines = [3, Inf];

%% Set up the Import Options and import the data
opts = spreadsheetImportOptions("NumVariables", 2);

% Specify sheet and range
opts.Sheet = sheetName;
opts.DataRange = data_col;

% Specify column names and types
opts.VariableNames = ["charge_Ah", "voltage_V"];
opts.VariableTypes = ["double", "double"];
opts.MissingRule = "omitrow";

% Import the data
ImportLG = readtable(workbookFile, opts, "UseExcel", false);
end
```

A.2 Process Cell Data

```
 %% Import From Excel
C02 = import_cell("Import LG.xlsx", "A3");
C2 = import_cell("Import LG.xlsx", "D3");
C5 = import_cell("Import LG.xlsx", "G3");
C15 = import_cell("Import LG.xlsx", "J3");
C20 = import_cell("Import LG.xlsx", "M3");
C30 = import_cell("Import LG.xlsx", "P3");

%Creating vector data

data = cell(6,1);
data{1} = C02;
data{2} = C2;
data{3} = C5;
data{4} = C15;
data{5} = C20;
data{6} = C30;

%Data treatment

for ii = 1:numel(data)
    table_temp = data{ii};
    capacity = linspace(0, table_temp.charge_Ah(end), 200).';
    voltage = interp1(table_temp.charge_Ah, table_temp.voltage_V, capacity, "linear
        ", "extrap");
    soc = capacity/capacity(end);
    data{ii} = table(capacity, voltage, soc);
end

%% Initial Plot

figure
plot(...
    data{1}.soc, data{1}.voltage, ...
    data{1}.soc, data{2}.voltage, ...
    data{1}.soc,data{3}.voltage, ...
    data{1}.soc,data{4}.voltage, ...
    data{1}.soc,data{5}.voltage, ...
    data{1}.soc,data{6}.voltage)
xlabel('DoD');
ylabel('Cell Voltage (V)');
title('Voltage vs DoD');
```

A.3 Power Dissipation Model: Energy Difference Vs Resistance Method

```
 %% Time and Power Calculations

% process

T02=(data{1}.capacity.*3600)./0.2;
T2=(data{2}.capacity.*3600)./2;
T5=(data{3}.capacity.*3600)./5;
T15=(data{4}.capacity.*3600)./15;
T20=(data{5}.capacity.*3600)./20;
T30=(data{6}.capacity.*3600)./30;

P02=data{1}.voltage.*0.2;
P2=data{2}.voltage.*2;
P5=data{3}.voltage.*5;
P15=data{4}.voltage.*15;
P20=data{5}.voltage.*20;
P30=data{6}.voltage.*30;

%% Internal Resistances

R2=(data{1}.voltage-data{2}.voltage)./(2-0.2);
R5=(data{1}.voltage-data{3}.voltage)./(5-0.2);
R15=(data{1}.voltage-data{4}.voltage)./(15-0.2);
R20=(data{1}.voltage-data{5}.voltage)./(20-0.2);
R30=(data{1}.voltage-data{6}.voltage)./(30-0.2);

figure
plot(...
    data{1}.soc, R2, ...
    data{1}.soc, R5, ...
    data{1}.soc,R15, ...
    data{1}.soc,R20, ...
    data{1}.soc,R30 ...
 )

Pd2=R2.*(2^2);
Pd5=R5.*(5^2);
Pd15=R15.*(15^2);
Pd20=R20.*(20^2);
Pd30=R30.*(30^2);

% Mean Power

mp2 = trapz(T2,Pd2) / T2(end);

mp5 = trapz(T5,Pd5) / T5(end);
```

```

mp15 = trapz(T15,Pd15) / T15(end);

mp20 = trapz(T20,Pd20) / T20(end);

mp30 = trapz(T30,Pd30) / T30(end);

% Power dissipation vector

Pd=[mp2 mp5 mp15 mp20 mp30];

%% Energy Difference

E02=trapz(T02, P02);
E2=trapz(T2, P2);
E5=trapz(T5, P5);
E15=trapz(T15, P15);
E20=trapz(T20, P20);
E30=trapz(T30, P30);

El2=E02-E2;
El5=E02-E5;
El15=E02-E15;
El20=E02-E20;
El30=E02-E30;

Pl2=El2/T2(end);
Pl5=El5/T5(end);
Pl15=El15/T15(end);
Pl20=El20/T20(end);
Pl30=El30/T30(end);

% Power loss vector

Pl=[Pl2 Pl5 Pl15 Pl20 Pl30];

%% Result Plots

I=[2,5,15,20,30];

plp=polyfit(I,Pl,3);
plxi=@(x) plp(1).*x.^3+plp(2).*x.^2+plp(3).*x+plp(4);

pdp=polyfit(I,Pd,2);
pdxi=@(x) pdp(1).*x.^2+pdp(2).*x+pdp(3);



figure;
fplot(plxi,[0,30]);
```

```
hold on;
fplot(pdxi,[0 30]);
xlabel('I (A)');
ylabel('Power Dissipation (W)');
title('Power Dissipation vs Current');
grid on;
```

A.4 Endurance Power Demand

```
 %CURRENT PATTERN

%% Data treatment

xi=380;
xf=10490;

xa=12000;
xb=22394;

dif=xf-xi;

delta=xb-xa;

% Import values
t = BMS1_VCU_MSG_04_BattCurrLem_00.time;
I = BMS1_VCU_MSG_04_BattCurrLem_00.signals.values;

C=I(xa:xb);
T=t(xa:xb);
I = I(xi:xf);
t = t(xi:xf);


% Savitzky-Golay Filter
windowSize = 11; % Size of filt window
polynomialOrder = 5; % Polynomial Order
Ip = sgolayfilt(I, polynomialOrder, windowSize);


Cp = sgolayfilt(C, polynomialOrder, windowSize);

% Plot to compare signals
figure;
plot(t, I, '-', 'DisplayName', 'Telemetry');
hold on;
plot(t, Ip, '--', 'DisplayName', 'Smoothed');
```

```
hold off;
xlabel('Time (s)');
ylabel('Current (A)');
legend;
title('Savitzky-Golay Filt');
grid on;

%% Calculation of Weighted Average Current

element=10; % multiples of 5

groups=floor(dif/element); %1st part
groupC=floor(delta/element); %2nd part

Iavg=[0,0];
Cavg=[0,0];
a=1-element;

for j=1:groups
    a=a+element;
    b=a+element-1;

    Iavg(j)=trapz(t(a:b),Ip(a:b))/(element/10);

end

a=1-element;

for j=1:groupC
    a=a+element;
    b=a+element-1;

    Cavg(j)=trapz(T(a:b),Cp(a:b))/(element/10);

end

%% Conversion to the Power loss functions

plg=@(x) 0.0019.*x.^3-0.0247.*x.^2+0.5608.*x-0.8489; % Function for the LG cells

lg=[0,0];
lg2=[0,0];

for i=1:groups
    lg(i)=plg(Iavg(i));
end

lg=abs(lg);

```

```
for i=1:groupC
    lg2(i)=plg(Cavg(i));
end

lg2=abs(lg2);

Power=sum(lg*element)/(element*groups);
time=element*groups/10;

PowerC=sum(lg2*element)/(element*groupC);
timeC=element*groupC/10;


figure
plot(Iavg)
hold on
plot(Cavg)
grid on
legend('First half','Second half')
xlabel('time step (s)')
ylabel('Current (I)')
title('Current Average vs Time Step')

figure
plot(lg)
hold on
plot(lg2)
grid on
legend('First half','Second half')
xlabel('time step (s)')
ylabel('Power Dissipation (W)')
title('Power Dissipation vs Time Step')
```

Appendix B

EES Implementation

```
 "Air Properties @30 C"

rho=density(Air;T=tm;P=100)
cp_air=cp(Air;T=tm)*1000
Pr=prandtl(Air;T=tm)
niu=viscosity(Air;T=tm)
k=conductivity(Air;T=tm)

tm=(te+ti)/2

"Cell"
mass=0,048
d=0,018
l=0,065
st=d+at
at=0,002
as=n*PI*d*l
cp_cell=953

nl=28
nt=4
n=nl*nt

"Temperatures"

ti=29

te=ts-(ts-ti)*exp((-as*h)/(m_dot*cp_air))

q_dot_cell=9,50

prod=(q_dot_cell-(q_dot_air/n))*dtime
ts=ti+(prod)/(mass*cp_cell)
```

```

Prrs=prandtl(Air;T=ts)


dtlm=((ts-te)-(ts-ti))/ln((ts*0,01)/(ts-ti))


"Calculatios"
 v=13,96
vmax=st*v/(st-d)
Re=rho*vmax*d/niu

Nu=0,27*(Re^0,63)*(Pr^0,36)*((Pr/Prs)^0,25)
h=Nu*k/d

m_dot=rho*(nt*st*l)*v
q_dot_air=h*as*dtlm
```